

SPT-3G lensing x DES Y3 shear

Aaron Ouellette* and SPT-3G Collaboration
(Dated: February 2, 2026)

The weak lensing of galaxies and of the cosmic microwave background (CMB) provide direct probes of the cosmic matter density field, but are sensitive to different redshift ranges and different survey systematics. Their cross-correlation is then able to provide consistency checks of the theoretical model and survey systematics. We present measurements of the CMB lensing - cosmic shear cross-correlation using new SPT-3G D1 lensing maps and the Y3 shear catalogs from the Dark Energy Survey (DES). For the first time, we detect this cross-correlation at high significance ($\sim 13\sigma$) when using a polarization-only CMB lensing reconstruction that is expected to be immune to extragalactic foregrounds. We also test a variety of other CMB lensing estimators that exhibit different tradeoffs between foreground biases and noise, as well as a pure blue shear sample that is expected to be less impacted by intrinsic alignments (IA). Assuming Λ CDM and marginalizing over IA, baryonic feedback, and various nuisance parameters, we obtain a constraint on the amplitude of matter clustering $S_8 \equiv \sigma_8 \sqrt{\Omega_m / 0.3} = 0.829^{+0.050}_{-0.064}$, consistent with both the primary CMB results from *Planck* and shear-only results from DES Y3. By combining our measurement with *Planck*, we show that it has some sensitivity to small-scale physics and obtain a constraint on the IA amplitude of the DES sample that is competitive with that from shear-only analyses as well as a lower limit on the strength of baryonic feedback.

I. INTRODUCTION

Gravitational lensing of distant light sources by the intervening large-scale structure (LSS) provides a wealth of information about the contents and evolution of the Universe since it is sensitive to both the cosmic expansion rate and the growth of structure [1, 2]. Additionally, one of the main strengths of weak lensing as a cosmological probe is that it provides an unbiased tracer of the matter density field, in contrast to galaxy clustering which has a very complicated connection to the underlying matter field.

The weak lensing signal has now been measured at high significance using both galaxies and the cosmic microwave background (CMB) as sources. On the galaxy lensing (also referred to as cosmic shear) side, Stage-III surveys, the Dark Energy Survey (DES), the Kilo-Degree Survey (KiDS), and the Hyper Suprime-Cam (HSC) survey, have been placing tight constraints on the amplitude of matter clustering at low redshift [3–6]. On the CMB lensing side, all major surveys, *Planck*, the Atacama Cosmology Telescope (ACT), and the South Pole Telescope (SPT), have achieved comparable constraints that are sensitive to significantly higher redshifts and larger physical scales [7–10].

With increasingly precise measurements of the amplitude of matter clustering across redshifts, a potential mild tension has emerged in the inferred value of the parameter $S_8 \equiv \sigma_8 \sqrt{\Omega_m / 0.3}$, where Ω_m is the fractional matter density and σ_8 parametrizes the amplitude of present-day density fluctuations. This so-called S_8 -tension is typically presented as a consistent trend where cosmic shear surveys measure the value of S_8 to be ~ 2

³⁶ to 3σ low relative to the Λ CDM prediction based on measurements of the primary CMB. This tension can be more precisely thought of as a mismatch between the amplitude of clustering on large and on small scales [11, 12].
⁴⁰ While many recent studies have shown that the S_8 tension can be resolved by allowing very strong baryonic feedback effects that suppress the matter power spectrum on small scales [], other explanations such as ...
⁴⁴ have been proposed []. This provides motivation to measure S_8 using a variety of probes that are sensitive to different ranges of redshifts and scales.

⁴⁷ Due to the fact that galaxy lensing and CMB lensing analyses use independent data sets with very different systematics, combined they provide very useful consistency checks of the standard Λ CDM model.

⁵¹ A major concern in CMB lensing measurements is contamination from extragalactic foregrounds that can mimic the lensing signal [13]. The main foregrounds include the Sunyaev-Zeldovich effects (both thermal, tSZ, and kinetic, kSZ), the cosmic infrared background (CIB), and radio sources. While a variety of techniques exist that aim to mitigate the impact of foregrounds on the reconstruction of CMB lensing maps, the foreground biases are expected to be worse when cross-correlating CMB lensing with low-redshift probes. This is due to the fact that the foregrounds are correlated with low-redshift LSS.

⁶³ Previous analyses: [14–16], DESxACT [17], DESxSPT [18–20]

⁶⁵ In this work, we measure the cross-correlation between CMB lensing and cosmic shear using new CMB lensing reconstructions based on data from SPT [21] and the DES Y3 shear catalog. We obtain the first high-significance measurement ($\sim 13\sigma$) of this cross-correlation using a CMB polarization-only lensing reconstruction, allowing us to effectively sidestep the issue of extragalactic foregrounds. We use this measurement as

* aaronjo2@illinois.edu

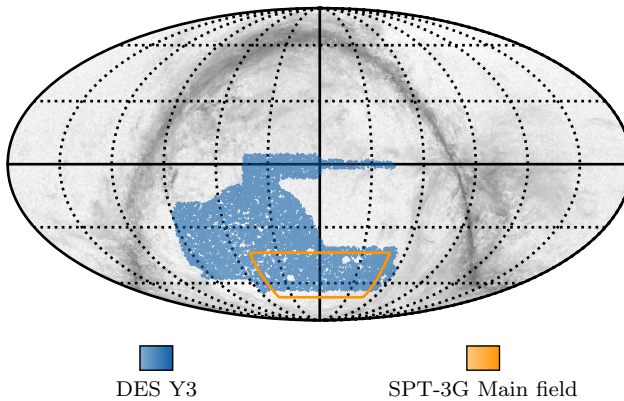


FIG. 1. Survey footprints for DES Y3 and the SPT-3G Main field in equatorial coordinates. Galactic dust as measured by *Planck* is shown in the background. The overlapping region covers approximately 1,300 deg².

73 a baseline to then asses different foreground mitigation
74 techniques when including CMB temperature data in the
75 lensing reconstruction. We additionally use a high-purity
76 sample of blue star-forming galaxies selected from the
77 DES Y3 catalog [22] that is expected to have an IA am-
78 plitude consistent with zero as a consistency check on our
79 modelling of IA.

80 This paper is structured as follows. We provide an
81 overview of the data used in Section II. We describe the
82 simulations used to validate our analysis in Section III.
83 In Section IV we describe our measurement of the CMB
84 lensing - cosmic shear cross-correlation. Section V pro-
85 vides details on the modelling and parameter inference.
86 We present the results in Section VII and conclude in
87 Section VIII.

88 Throughout, when assuming a fiducial cosmology, we
89 use values consistent with the *Planck* 2018 flat Λ CDM
90 results [23].

II. DATA

A. SPT-3G CMB lensing maps

93 The CMB lensing maps used in this work are presented
94 in [21]. Here we provide a quick overview of the data used
95 to construct the lensing maps and the different recon-
96 struction techniques used to mitigate foreground biases.

97 SPT-3G [24] is the third generation camera installed
98 on the South Pole Telescope [25] and has been in opera-
99 tion since 2018. The lensing maps used here are based on
100 temperature and polarization observations made during
101 the 2019 and 2020 winter seasons. The main SPT-3G
102 survey field covers a 1500 deg² patch in the Southern sky
103 as shown in Fig. 1 and achieves average coadded noise

104 levels of 3.3 (5.1) μ K-arcmin in temperature (polariza-
105 tion) [26].

106 CMB lensing maps are generally reconstructed from
107 the primary CMB maps using some form of a quadratic
108 estimator (QE). In this work, we consider five different
109 variants that have different tradeoffs between foreground
110 mitigation and noise.

- 111 1. Global minimum variance (GMV) map. This is
112 an extension of the standard quadratic estimator
113 (SQE) that was first introduced by [27]. The GMV
114 estimator was derived by [28] and incorporates cor-
115 relations between the CMB temperature and polar-
116 ization fields that are neglected in the traditional
117 SQE.
- 118 2. Polarization-only QE map. This reconstruction
119 only uses polarization information and is expected
120 to be immune to extragalactic foreground biases
121 due to the fact that they are essentially unpolarized.
122 [refs on limits of foreground polarization: [29–
123 31]]
- 124 3. Profile hardened GMV map. Profile-hardening (or
125 bias-hardening) [13, 32] modifies the QE to make
126 it insensitive to contributions from the trispectra of
127 some assumed source profiles such as galaxy clus-
128 ters and radio sources.
- 129 4. Gradient-cleaned GMV [33] and
- 130 5. Cross-ILC GMV map. This estimator uses the
131 internal linear combinations (ILC) algorithm to con-
132 struct tSZ-nulled and CIB-nulled CMB maps which
133 are then used as input in the QE [34].

134 The gradient-cleaned and cross-ILC estimators are imple-
135 mented on top of the GMV (rather than SQE) estimator
136 using the formalism of [35].

137 We refer to these five lensing reconstruction variants
138 as ‘GMV’, ‘Pol’, ‘Prof’, ‘MH’, and ‘xILC’, respectively.
139 Of these variants, the GMV reconstruction is expected to
140 have the lowest noise, especially on small scales, but be
141 the most impacted by foregrounds. The Pol reconstruc-
142 tion is expected to be the most robust to foregrounds
143 while having significantly higher noise on small scales.
144 The other variants all include temperature information
145 and employ some foreground mitigation technique in or-
146 der to attempt to extract more lensing signal while re-
147 maining unaffected by foreground biases.

B. DES Y3 shear catalog

149 The Dark Energy Survey (DES) has observed about
150 5,000 deg² of the Southern sky in five photometric bands
151 (*grizY*) [36–38]. The observations were taken using the
152 DECam [39] camera on the Blanco telescope at the Cerro
153 Tololo Inter-American Observatory in Chile.

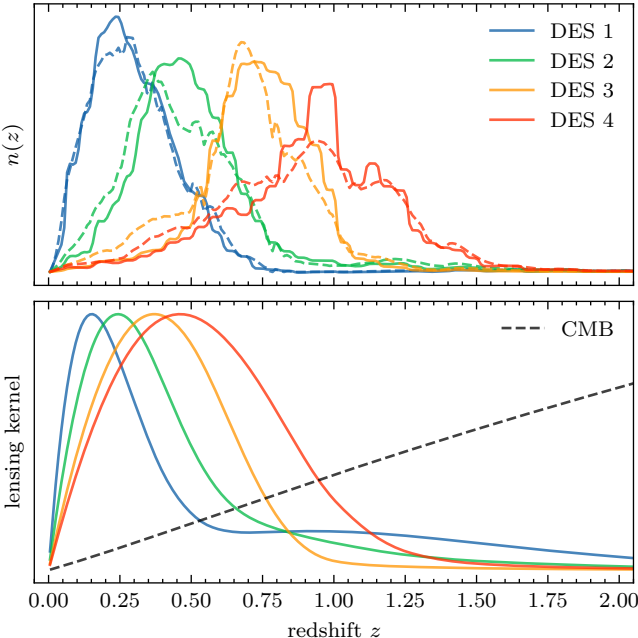


FIG. 2. Top panel: Redshift distributions of the four DES Y3 tomographic bins. Solid lines represent the full sample while dashed lines represent the blue subsample. Bottom panel: The corresponding lensing kernels for the full DES Y3 sample compared to the lensing kernel of the CMB (black dashed line). The kernels for the blue subsample are qualitatively very similar to those of the full sample. All kernels have been normalized to unit height.

In this work we use the publicly released catalogs¹ based on data from the first three years of observations (Y3). This is a subset of the Gold catalog [40] and consists of 100 million galaxies with shape measurements [41] and divided into 4 tomographic bins using photometric redshifts [42]. The redshift distributions of the DES Y3 tomographic bins are shown in the top panel of Fig. 2.

Additionally, we use the blue subsample of the DES Y3 data derived and analyzed by [22]. This subsample was developed with the goal of obtaining a pure sample of blue star-forming galaxies that are expected to be less impacted by intrinsic alignments than a mixed sample. We use the publicly released sample selection² to generate the blue catalogs and use the updated redshift distributions and calibrations that are presented in [22] when analyzing this sample.

We calibrate each of the shear catalogs using the METACALIBRATION algorithm [43, 44]. For each tomographic bin, we subtract the mean ellipticity and correct by the multiplicative shear bias to obtain calibrated

galaxy shear estimates γ_i from the galaxy shape measurements e_i :

$$\hat{\gamma}_i = \frac{1}{\langle R \rangle} (e_i - \langle e \rangle), \quad (1)$$

where $R = R_\gamma + R_s$ is the combination of the shear response and selection response. This calibration is calculated from the catalogs as detailed in [41].

In Table I we provide an overview of the properties and calibration values of the four tomographic bins for both the full DES Y3 shear sample and the blue subsample.

III. SIMULATIONS

To validate our measurement and analysis pipelines, we use the AGORA³ simulations [45] which are based on the MULTIDARK-PLANCK2 (MDPL2) [46] N -body simulation. AGORA uses the halos and particles from MDPL2 to generate lightcones, full-sky fields, and mock observations for a variety of observables. AGORA consists of a single full-sky realization which we split into 10 independent patches that each cover the same sky area as the SPT-3G main field.

A. Mock DES Y3 shear catalogs

The AGORA full-sky galaxy weak lensing signal maps [45] were generated to match the actual DES Y3 redshift distributions and include a level of intrinsic alignments that is consistent with the results of [47]. We generate simulated shear catalogs from the full-sky maps by sampling the signal at the locations of galaxies in the DES Y3 catalog. These noiseless catalogs are used to test for potential bias in the measured cross-correlation. We additionally incorporate realistic shape noise by randomly rotating the shear measurements of the DES Y3 catalog and adding the resulting noise to the noiseless catalogs. These realistic catalogs allow us to test the estimated covariance matrix of the measured cross-correlations.

B. Mock SPT-3G lensing maps

Since foreground contamination is expected to be a problem when cross-correlating temperature-based lensing maps with low-redshift tracers such as cosmic shear, it is important to use realistic simulations that include this effect in order to quantify the potential impact on cosmological parameter inference. AGORA includes full non-Gaussian realizations of the tSZ, kSZ, and CIB fields that are included when generating mock observations of the CMB field. Full details on the construction of these mock lensing maps can be found in [21, 45].

¹ <https://des.ncsa.illinois.edu/releases/y3a2/>

² **Y3key-catalogs.** Note that we use the updated SOMPP v0.50 photometric catalog which corrects the tomographic bin placement for some galaxies. See also footnote 5 in [22].

³ <https://yomori.github.io/agora/index.html>

Bin	N_{gal}	R_γ	R_s	$\langle z \rangle$	$\sigma_{\Delta z}$	$\langle m \rangle$	σ_m
Full 1	24,882,718	0.763	0.005	0.33	0.018	-0.0063	0.0091
Full 2	25,224,643	0.719	0.008	0.52	0.015	-0.0198	0.0078
Full 3	24,831,367	0.693	0.012	0.74	0.011	-0.0241	0.0076
Full 4	25,265,298	0.609	0.015	0.93	0.017	-0.0369	0.0076
Blue 1	18,031,829	0.760	0.007	0.36	0.018	-0.0129	0.0091
Blue 2	16,670,470	0.713	0.012	0.52	0.015	-0.0180	0.0078
Blue 3	12,233,530	0.696	0.018	0.70	0.011	-0.0203	0.0076
Blue 4	18,130,765	0.618	0.015	0.90	0.017	-0.0356	0.0076

TABLE I. Properties and calibration parameters for the full DES Y3 shear sample and the blue subsample. For each tomographic bin we list the number of galaxies (N_{gal}), the average shear and selection responses (R_γ , R_s), the average redshift ($\langle z \rangle$), the uncertainty on the shift in the mean redshift ($\sigma_{\Delta z}$), the residual shear calibration ($\langle m \rangle$), and the uncertainty on the shear calibration (σ_m).

217

IV. MEASUREMENT

218

A. Shear map making

We generate shear maps and associated masks from the calibrated DES Y3 catalogs following [48, 49]. Through-out, we use the HEALPix pixelization scheme as implemented in HEALPY [50, 51] with a resolution parameter of $N_{\text{side}} = 2048$.

The average shear γ at pixel p is given by

$$\gamma_p = \sum_{i \in p} v_i \gamma_i / \sum_{i \in p} v_i, \quad (2)$$

where γ_i and v_i are the shear and measurement weight (which is assumed to be approximately an inverse variance weight) respectively of the i -th galaxy.

The mask associated with the shear maps is simply given by the sum of weights map

$$w_p = \sum_{i \in p} v_i. \quad (3)$$

230

B. Power spectra

Cosmic shear γ is a spin-2 field and can be decomposed into E - and B -modes [52]. The harmonic-space cross-correlation of cosmic shear with the scalar CMB lensing field κ then has two components: $C_\ell^{\kappa\gamma_E}$ and $C_\ell^{\kappa\gamma_B}$. At linear order, weak lensing by LSS does not generate B -modes, so our measurement mainly concerns $C_\ell^{\kappa\gamma_E}$, while $C_\ell^{\kappa\gamma_B}$ is expected to be consistent with zero. For simplicity, we will generally refer to $C_\ell^{\kappa\gamma}$ which is assumed to be the E -mode cross-spectrum unless otherwise noted.

We use NAMASTER⁴ [53], which implements the pseudo- C_ℓ or MASTER algorithm [54] for arbitrary spin

fields, to measure the mask-deconvolved cross-spectra $C_\ell^{\kappa\gamma}$ from the masked shear γ and CMB lensing κ maps. The mask applied to the CMB lensing maps is effectively three powers of an apodized border mask resulting from the quadratic estimator reconstruction process and an additional point source mask that is constructed from a list of detected point sources and galaxy clusters as described in [21]. The mask applied to the shear field is the map of inverse-variance weights as given by Eq. (3).

The full details of the pseudo- C_ℓ method for general fields are given in [53] and its specific application to cosmic shear is described in [48]. Here we provide a brief description. For masked observed fields $\tilde{\gamma}$ and $\tilde{\kappa}$, the E -mode pseudo-cross-spectrum is defined as

$$\tilde{C}_\ell^{\kappa\gamma} = \frac{1}{2\ell+1} \sum_m \tilde{\gamma}_{\ell m}^E \tilde{\kappa}_{\ell m}^*. \quad (4)$$

The pseudo-cross-spectrum is related to the underlying true cross-spectrum through a mode-coupling matrix $M_{\ell\ell'}$:

$$\langle \tilde{C}_\ell^{\kappa\gamma} \rangle = \sum_{\ell'} M_{\ell\ell'} C_\ell^{\kappa\gamma}. \quad (5)$$

The coupling matrix depends only on the masks applied to the two fields and the field spin values (see [53] for the full expressions). We additionally correct the pseudo-cross-spectra by one power of the HEALPIX pixel window function to account for the pixelization of the shear maps.

In order to invert the mode-coupling matrix, NAMASTER bins the cross-spectra into bandpowers. We choose to use the following binning scheme: 6 linear bins over the range $30 \leq \ell \leq 246$ and 18 logarithmic bins over the range $246 \leq \ell \leq 3500$. The minimum and maximum values of ℓ are given by the range of angular multipoles included in the lensing reconstruction. CC: justification of these scales AO: sufficient justification? scale cuts are covered later The mix of linear and logarithmic binning allows us to have somewhat finer bins on large scales where the signal is the largest and wider bins on small

⁴ <https://namaster.readthedocs.io/en/latest/>

276 scales where the noise in the CMB lensing maps increases
 277 substantially.

278 We calculate the Gaussian part of the bandpower co-
 279 variances using the improved narrow kernel approxima-
 280 tion (iNKA) as described in [48, 55] and implemented
 281 in NAMASTER. The covariances are calculated directly
 282 from the mode-coupled pseudo- C_ℓ s and do not rely on a
 283 theory prediction for the cross-spectra in order to avoid
 284 any mis-modeling of signal and noise on small scales.

285 We show the resulting cross-correlation bandpowers in-
 286 volving the full DES Y3 shear sample in Fig. 3 and involv-
 287 ing the blue subsample in Fig. 4. We find no evidence for
 288 non-zero cross-spectra with the shear B -modes. The full
 289 shear B -mode cross-spectra are shown in Appendix A.

290 V. ANALYSIS

291 A. Modelling

292 In the Limber approximation [56, 57] (valid on scales
 293 $\ell \gtrsim 20$) lensing cross-correlations are given by

$$294 C_\ell^{ij} = \int \frac{d\chi}{\chi^2} W_i(\chi) W_j(\chi) P_m[k_\ell(\chi), z(\chi)], \quad (6)$$

294 where $k_\ell(\chi) \equiv (\ell + 1/2)/\chi$, χ is the comoving radial dis-
 295 tance, and $P_m(k, z)$ is the 3D matter power spectrum.
 296 The indices i, j refer to the different tracers or tomo-
 297 graphic bins that are being cross-correlated and W_i is
 298 the corresponding lensing kernel.

299 For a sample of galaxies with redshift distribution $n(z)$,
 300 the lensing convergence (κ) kernel is

$$337 W_\kappa^i(\chi) = \frac{3}{2} \Omega_m H_0^2 \frac{\chi}{a(\chi)} \int_{\chi}^{\infty} d\chi' n_i(\chi') \frac{\chi - \chi'}{\chi'}. \quad (7)$$

301 For galaxy lensing, the direct observable is the reduced
 302 shear $\mathbf{g} = \boldsymbol{\gamma}/(1 - \kappa)$, rather than the lensing conver-
 303 gence κ . But, in the weak lensing regime ($\kappa \ll 1$) and
 304 at the current levels of sensitivity, the difference between
 305 reduced shear and shear can be neglected [49]. Addi-
 306 tionally, the difference between the E -mode shear power
 307 spectrum and the convergence power spectrum is only an
 308 ℓ dependent prefactor that is ~ 1 on scales $\ell \gtrsim 20$ and
 309 can also be neglected in this analysis. Finally, as in most
 310 analyses, we do not model the shear B -mode power spec-
 311 trum since it is below the current detection threshold.

312 The CMB is very well approximated by a single source
 313 at $\chi = \chi_*$, where χ_* is the distance to the surface of last
 314 scattering, so the CMB lensing kernel becomes

$$354 W_\kappa^{\text{CMB}}(\chi) = \frac{3}{2} \Omega_m H_0^2 \frac{\chi}{a(\chi)} \frac{\chi - \chi_*}{\chi_*}. \quad (8)$$

315 We use CAMB [58, 59] and HMCode [60] to calculate
 316 the non-linear matter power spectrum.

1. Intrinsic alignments

318 Due to tidal forces, galaxies are not randomly oriented,
 319 but tend to align with the large-scale tidal field, leading
 320 to an additional contribution to the shear power spec-
 321 trum. Intrinsic alignments are one of the main sources
 322 of systematic uncertainty in the modelling of shear data
 323 and many methods have been developed to model their
 324 contribution (see [61, 62] for reviews).

325 The DES Y3 analysis used the tidal alignment and
 326 tidal torquing (TATT) model [63], which includes second-
 327 order effects, as their fiducial analysis choice, but showed
 328 that the simpler nonlinear linear alignment (NLA) model
 329 [64, 65] was sufficient to model the DES Y3 data [66].
 330 Since the cross-correlations with CMB lensing are less
 331 constraining than the shear auto-spectra, we use the sim-
 332 pler NLA model in this analysis.

333 The NLA model assumes that the IA power spectrum
 334 is linearly proportional to the matter power spectrum. In
 335 this model, we simply add an extra term to the galaxy
 336 lensing kernel:

$$337 W_\kappa^i(\chi) \rightarrow W_\kappa^i(\chi) + W_{\text{IA}}^i(\chi). \quad (9)$$

$$337 W_{\text{IA}}^i(\chi) = -A_1 C_1 \rho_{\text{crit}} \frac{\Omega_m}{D(z)} n_i(\chi) \left(\frac{1+z}{1+z_0} \right)^{\alpha_1}, \quad (10)$$

338 where $D(z)$ is the linear growth factor, $C_1 = 5 \times 10^{-14} h^{-2}$
 339 $M_\odot^{-1} \text{Mpc}^3$ is a normalization constant, $z_0 = 0.62$, and
 340 A_1 and α_1 are free parameters that determine the IA
 341 amplitude and redshift evolution respectively.

342 When modelling cross-correlations with the Blue shear
 343 sample, we assume zero IA amplitude as done in [22].

2. Baryonic feedback

345 Baryonic feedback is a major source of theoretical un-
 346 certainty in the small scales ($k \gtrsim 1 h \text{ Mpc}^{-1}$) of the
 347 nonlinear matter power spectrum [67]. Instead of ap-
 348 plying scale cuts to the data that remove sensitivity to
 349 these scales, we account for this uncertainty by marginal-
 350 izing over the $\log T_{\text{AGN}}$ parameter in HMCode. This
 351 parameterization was calibrated to reproduce the matter
 352 power spectrum observed in the BAHAMAS hydrodyna-
 353 mical simulations [68].

3. Shear measurement uncertainties

355 As in the official DES Y3 analysis [49], we marginal-
 356 ize over uncertainties in the shear calibration and the
 357 redshift distributions of the source galaxies.

358 Uncertainties in the redshift distributions are parame-
 359 terized through a shift Δz_i of their means:

$$359 n_i(z) \rightarrow n_i(z + \Delta z_i). \quad (11)$$

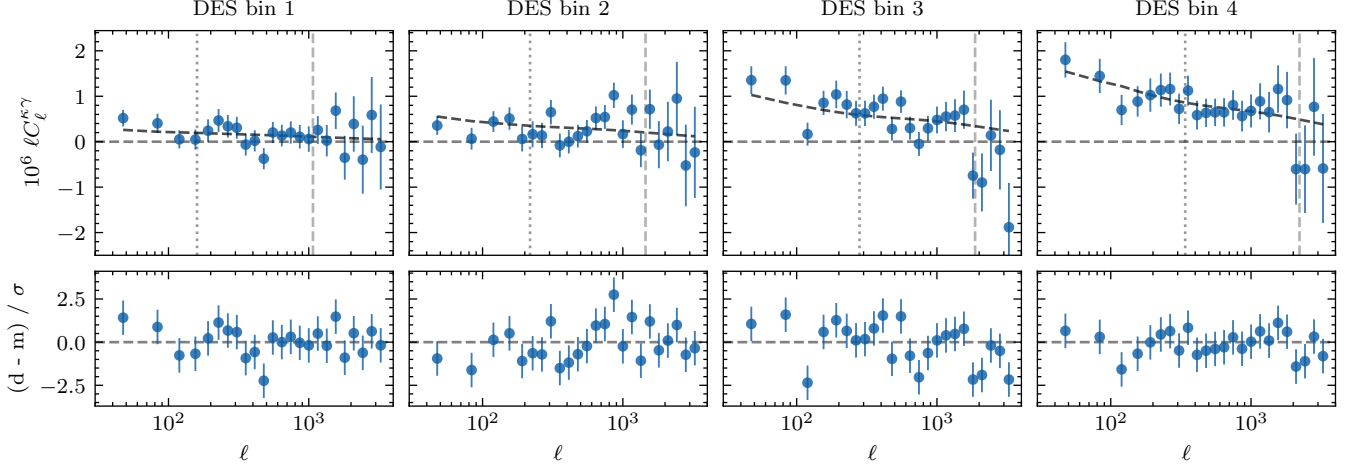


FIG. 3. Measured $C_\ell^{\kappa\gamma}$ cross-correlation bandpowers using the SPT-3G polarization-only lensing reconstruction and the full DES Y3 shear sample. The black dashed lines show the best fit model using all scales and the bottom panels show the residuals relative to this model. The grey vertical lines indicate the ℓ values corresponding to scale cuts of $k_{\text{max}} = 5h \text{ Mpc}^{-1}$ (dashed) and $1h \text{ Mpc}^{-1}$ (dotted) (see Section V B 3).

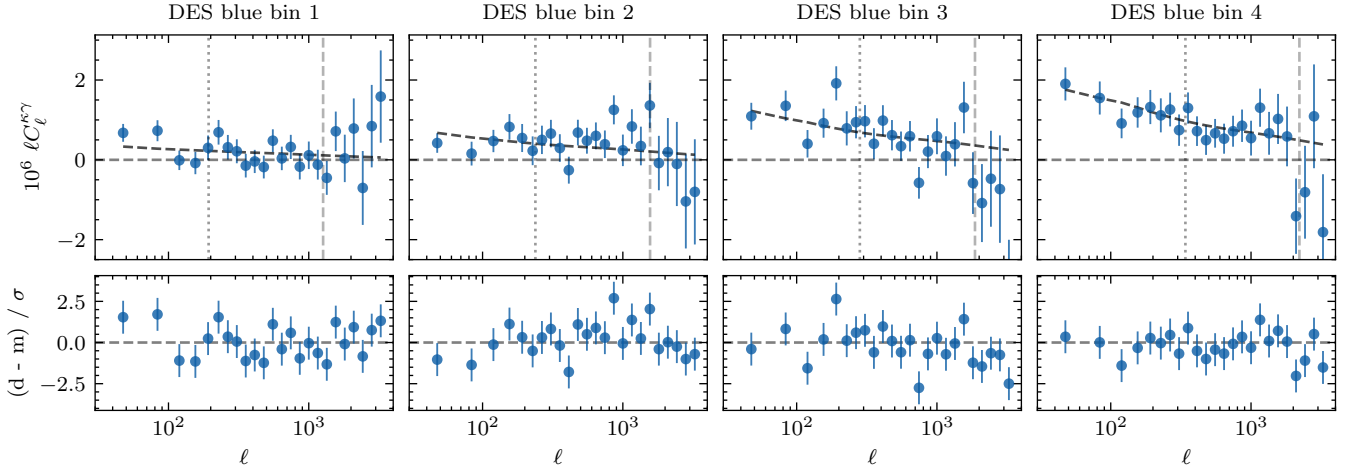


FIG. 4. Same as Fig. 3, but using the DES blue subsample.

Residual uncertainties in the shear calibration are parameterized using a constant amplitude m_i for each bin:

$$C_\ell^{\kappa\gamma_i} \rightarrow (1 + m_i) C_\ell^{\kappa\gamma_i}. \quad (12)$$

All of the redshift shift parameters Δz_i and shear calibration parameters m_i have tight Gaussian priors from detailed simulations of the DES data. Extensive testing in the official DES Y3 analyses has shown that these parameterizations of the measurement uncertainties are sufficiently accurate [69].

Since the shear calibration parameters m_i enter only as linear amplitudes on the cross-spectra, we choose to analytically marginalize over them in a similar manner to what is done in [70, 71]. This is accomplished by fixing m_i to the means of their priors and adding an additional term to the data covariance:

$$\text{Cov}_m(C_\ell^{\kappa\gamma_i}, C_{\ell'}^{\kappa\gamma_j}) = \sigma_i^2 \delta_{ij} C_\ell^{\kappa\gamma_i} C_{\ell'}^{\kappa\gamma_j}, \quad (13)$$

where σ_i is the Gaussian prior on m_i and the cross-spectra are computed at the fiducial model. This expression can be straightforwardly derived from the expressions in [70, 71] with slight modifications to account for the DES assumption of uncorrelated calibrations per tomographic bin and the fact that $m = 0$ for the κ field. We have verified that we get essentially identical results whether we use this analytic marginalization method or sample the m_i parameters.

4. Non-Gaussian covariance terms

We model the total covariance of the cross-spectra as the sum of the Gaussian covariance computed using NMASTER (C_G , Section IV B), the shear calibration term (C_m , Section V A 3), and two additional terms that ac-

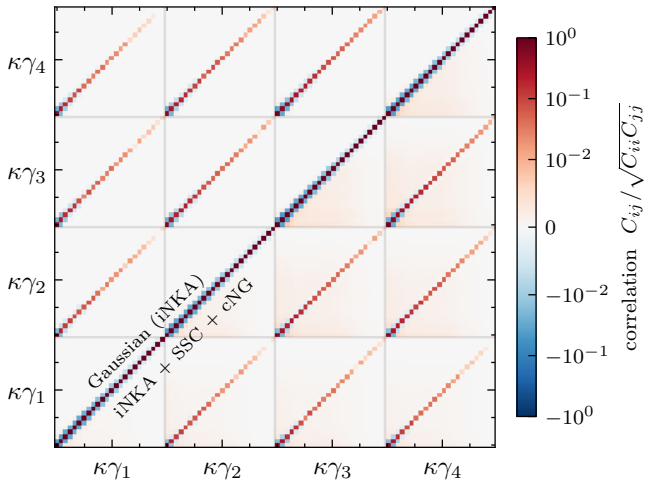


FIG. 5. Normalized data covariance matrix for the Full x Pol cross-correlation. The upper half of the matrix shows only the Gaussian part computed using NAMASTER, while the bottom half shows the full covariance, including the non-Gaussian components. The sub-blocks correspond to the cross-correlations between the CMB lensing (κ) and the individual DES tomographic bins (γ_i).

³⁸⁸ count for mode coupling from the non-Gaussianity of the
³⁸⁹ lensing field:

$$C = C_G + C_m + C_{SSC} + C_{cNG}. \quad (14)$$

³⁹⁰ C_{SSC} is the super-sample covariance term [72] that arises
³⁹¹ from modes larger than the survey mask. C_{cNG} is the
³⁹² connected non-Gaussian term [73] that arises from the
³⁹³ non-Gaussian matter trispectrum.

³⁹⁴ The SSC and cNG terms are calculated through a halo
³⁹⁵ model approximation implemented using the Core Cos-
³⁹⁶ mology Library (CCL) [74]. To construct the halo model,
³⁹⁷ we assume a NFW profile [75] for dark matter halos, use
³⁹⁸ the halo mass function and halo bias parameterizations
³⁹⁹ from [76], and the halo concentration relation from [77].

⁴⁰⁰ In theory, there should be another contribution to the
⁴⁰¹ total covariance due to the uncertainty in the fiducial
⁴⁰² cosmology used in the CMB lensing reconstruction. We
⁴⁰³ neglect this contribution as it is expected to be negligibly
⁴⁰⁴ small. **AO: need additional details about lensing response**
⁴⁰⁵ **function**

⁴⁰⁶ The full data covariance matrix is shown in Fig. 5.
⁴⁰⁷ Both the SSC and cNG terms are sub-dominant to the
⁴⁰⁸ Gaussian term, but the SSC term adds small off-diagonal
⁴⁰⁹ correlations on large scales. The cNG term is mostly
⁴¹⁰ negligible, but is still included for completeness.

Parameter	Fiducial value	Prior
Cosmology		
Ω_m	0.311	$\mathcal{U}(0.1, 0.9)$
Ω_b	0.049	$\mathcal{U}(0.03, 0.07)$
h	0.677	$\mathcal{U}(0.55, 0.91)$
$10^9 A_s$	2.105	$\mathcal{U}(0.5, 5)$
n_s	0.967	$\mathcal{U}(0.87, 1.07)$
m_ν	0.06 eV (fixed)	
Intrinsic alignments		
A_1	0.44	$\mathcal{U}(-5, 5)$
α_1	0.0	$\mathcal{N}(0, 2)$
Baryonic feedback		
$\log T_{AGN}$	7.8	$\mathcal{U}(7.3, 8.3)$
Shear calibration		
m_1	fixed to mean values in Table I and marginalized over analytically	
m_2		
m_3		
m_4		
Redshift uncertainties		
Δz_1	0.0	$\mathcal{N}(0, 0.018)$
Δz_2	0.0	$\mathcal{N}(0, 0.015)$
Δz_3	0.0	$\mathcal{N}(0, 0.011)$
Δz_4	0.0	$\mathcal{N}(0, 0.017)$

TABLE II. Summary of parameters and priors used in the analysis. $\mathcal{U}(a, b)$ indicates a uniform prior, while $\mathcal{N}(\mu, \sigma)$ indicates a Gaussian prior. When doing a joint analysis with the *Planck* likelihood, we additionally vary the optical depth τ using a prior $\mathcal{U}(0.01, 0.8)$.

B. Parameter inference

1. Priors

⁴¹¹ We sample all parameters over the same ranges used
⁴¹² in the DES Y3 analysis with a few small changes. We as-
⁴¹³ sume a single massive neutrino species with a fixed mass
⁴¹⁴ of $m_\nu = 0.06$ eV. For intrinsic alignments, we uniformly
⁴¹⁵ sample the amplitude A_1 over the range (-5, 5) and sam-
⁴¹⁶ ple the power law exponent using a Gaussian prior cen-
⁴¹⁷ tered at zero with width $\sigma = 2$. We choose to use a Gaus-
⁴¹⁸ sian prior for α_1 since this parameter is unconstrained by
⁴¹⁹ the data and very steep power laws are not expected to be
⁴²⁰ physically plausible. For the shear nuisance parameters
⁴²¹ m_i and Δz_i , we use the same Gaussian priors used in the
⁴²² official DES Y3 analyses. We sample the baryonic feed-
⁴²³ back parameter $\log T_{AGN}$ uniformly over the range (7.3,
⁴²⁴ 8.3). While HMCode was calibrated to match hydrody-
⁴²⁵ namical simulations over the range (7.6, 8.3), we extend
⁴²⁶ the range, following [4], in order to include low feedback
⁴²⁷ models that are roughly consistent with a gravity-only
⁴²⁸ model. We provide a summary of all the priors and fidu-
⁴²⁹ cial parameter values used in our parameter inference in
⁴³⁰ **431**

k_{\max} cut [$h \text{ Mpc}^{-1}$]	ℓ_{\max} cut (Full / Blue)				N_d
	bin 1	bin 2	bin 3	bin 4	
0.5	82	115	150	182	10
	99	126	151	183	12
1	160	218	281	340	24
	193	238	282	341	26
2	342	462	593	709	43
	409	501	593	710	45
5	1071	1451	1871	2216	75
	1266	1563	1867	2213	77

TABLE III. Conversion of k_{\max} cuts to ℓ_{\max} cuts, assuming the fiducial model listed in Table II. Due to the slightly different redshift distributions of the Full and Blue shear samples, a given k cut translates into slightly different ℓ cuts, especially for the first two tomographic bins. The last column lists the number of remaining data points N_d (out of the total of 96) after applying the scale cuts.

432 Table II.

433 2. Likelihood

434 We assume a Gaussian likelihood \mathcal{L} for the joint dis-
435 tribution of the cross-spectra bandpowers:

$$-2 \ln \mathcal{L} + K \equiv$$

$$\chi^2 = (\mathbf{d} - \mathbf{m}(\boldsymbol{\theta}))^T \mathbf{C}^{-1} (\mathbf{d} - \mathbf{m}(\boldsymbol{\theta})), \quad (15)$$

436 where K is an arbitrary constant, \mathbf{d} is the data vector
437 consisting of the measured cross-spectra, \mathbf{m} is the model
438 computed at given values of the parameters $\boldsymbol{\theta}$, and \mathbf{C}
439 is the covariance matrix of the data. The posterior is
440 then proportional to the product of the likelihood and
441 the prior:

$$P(\boldsymbol{\theta}|\mathbf{d}) \propto \mathcal{L}(\mathbf{d}|\boldsymbol{\theta}) P(\boldsymbol{\theta}). \quad (16)$$

442 The likelihood is implemented using the COSMOSIS⁵
443 framework [78] and we sample the posterior using the
444 nested sampler NAUTILUS⁶ [79]. Starting from the high-
445 est posterior sample in each NAUTILUS chain, we find the
446 maximum a posteriori (MAP) point using the Nelder-
447 Mead optimization algorithm as implemented in SCIPY
448 [80]. For each fit, we estimate the effective number
449 of parameters N_{eff} that are constrained relative to the
450 prior using the Gaussian approximation implemented
451 in TENSIOMETER⁷ [81]. This is then used to estimate
452 the goodness-of-fit by comparing the χ^2 value of the
453 MAP point to the estimated degrees of freedom $N_{\text{dof}} =$
454 $N_d - N_{\text{eff}}$, where N_d is the size of the data vector.

455 3. Scale cuts

456 For our fiducial analysis, we attempt to fit all scales
457 present in the measured data vectors ($30 \leq \ell \leq 3500$).
458 To test the robustness of our results, we also test the
459 effect of scale cuts designed to remove sensitivity to all
460 scales in k space $k > k_{\max}$. To convert a k_{\max} cut to a
461 corresponding ℓ_{\max} cut, we use a method similar to that
462 developed by [70]. Specifically, for a given cross-spectrum
463 we calculate the C_ℓ using the full nonlinear $P(k)$ and
464 using a $P(k)$ that has been exponentially suppressed for
465 $k > k_{\max}$. We then define ℓ_{\max} as the maximum value
466 of ℓ for which the two C_ℓ s agree within a given threshold
467 (here we choose 5%). The resulting scale cut ensures that
468 no more than 5% of the signal in the data vectors depends
469 on k modes beyond k_{\max} . Table III lists the specific ℓ_{\max}
470 cuts that correspond to $k_{\max} \in \{0.5, 1, 2, 5\} h \text{ Mpc}^{-1}$ for
471 each of the tomographic bins of the $\kappa\gamma$ cross-correlation
472 for both the Full and Blue samples.

473 There are two main components of the theory model
474 that are expected to be mis-modeled at some level in
475 this analysis: the matter power spectrum and galaxy IA.
476 Since HMCode has been calibrated against simulations
477 to roughly the per-cent level at $k < 20h \text{ Mpc}^{-1}$ and
478 $z < 1$ [60], systematic uncertainty in the matter power
479 spectrum is not expected to be significant compared to
480 the statistical uncertainty of our measurement. On the
481 other hand, it is reasonable to expect more significant
482 problems on the IA modeling side, since IA models are
483 generally not tested on nonlinear scales. While the model
484 that we use (NLA) is particularly simplistic, there is ev-
485 idence from simulations that it is roughly valid out to
486 $k \sim 1h \text{ Mpc}^{-1}$ [82].

487 We find that for all of the $\kappa\gamma$ data vectors, the total
488 bandpower SNR fully saturates by the scale cuts corre-
489 sponding to $k_{\max} = 5h \text{ Mpc}^{-1}$ and approximately 50% of
490 the total SNR comes from multipoles that are insensitive
491 to $k > 0.5h \text{ Mpc}^{-1}$. It is important to note that, due to
492 the very wide lensing kernels, a given range in ℓ receives
493 contributions from a wide range in k . This means that
494 applying a k_{\max} scale cut as described above removes
495 some sensitivity in the data to modes $k < k_{\max}$ in addi-
496 tion to removing the sensitivity to all modes $k > k_{\max}$.
497 Based on these considerations, we do not expect our fidu-
498 cial choice of including all multipoles to significantly bias
499 our results.

500 VI. VALIDATION

501 Using the AGORA simulated CMB lensing reconstruc-
502 tions and simulated shear catalogs, we conduct three
503 tests to validate our measurement and analysis. First,
504 using the simulated shear catalogs without shape noise,
505 we test for biases in the cross-correlation bandpowers.
506 We then include a realistic level of shape noise to test
507 our analytic estimate of the covariance matrix and to
508 test the analysis pipeline for correct parameter recovery.

⁵ <https://cosmosis.readthedocs.io/en/latest/>

⁶ <https://nautilus-sampler.readthedocs.io/en/latest/>

⁷ <https://tensiometer.readthedocs.io/en/latest/index.html>

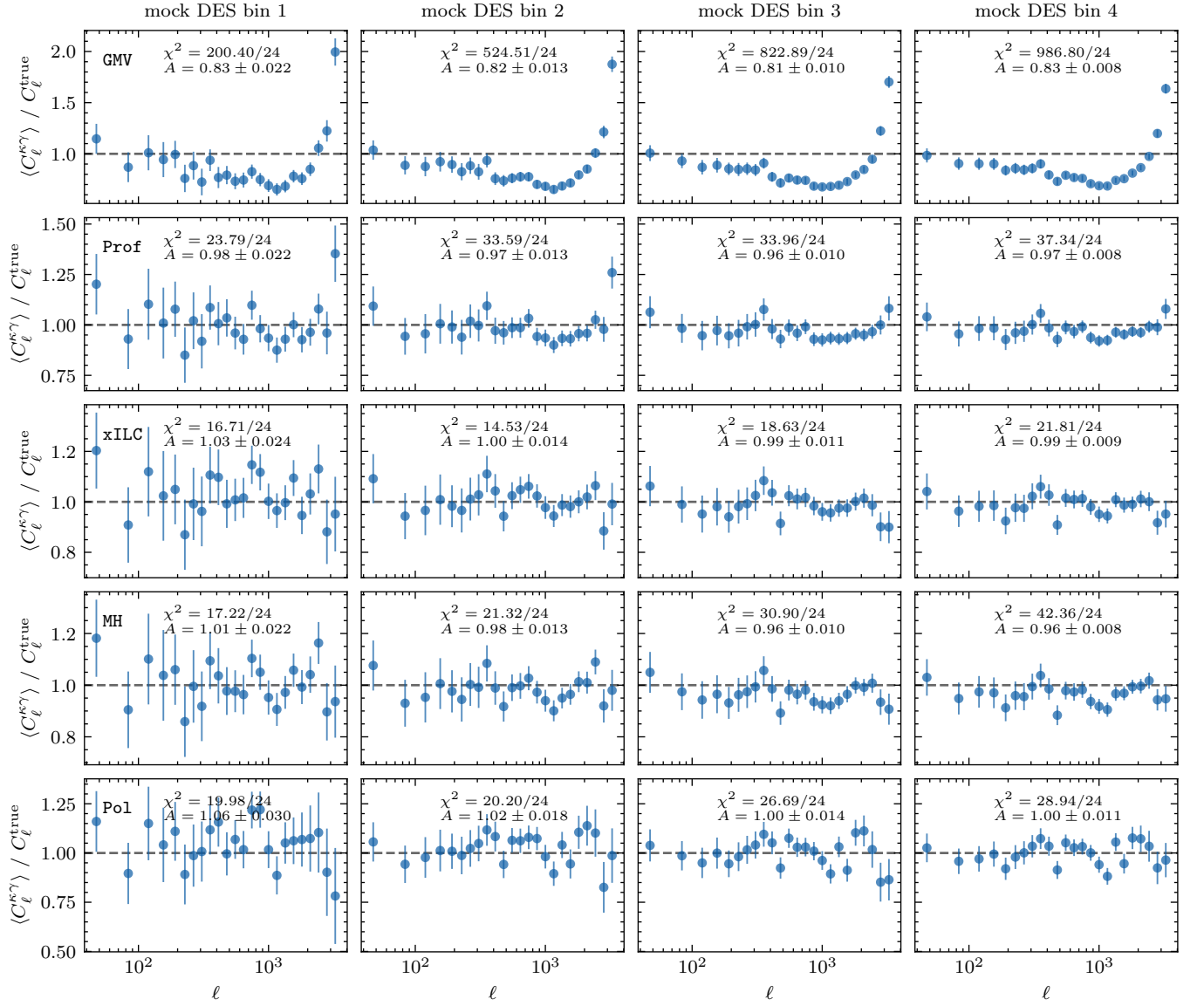


FIG. 6. Measurement validation on AGORA simulated data. Each panel compares the mean measured $\kappa\gamma$ cross-correlation to the truth (measured over the full sky with no noise). Each column corresponds to a different tomographic bin, while each row corresponds to a different CMB lensing reconstruction. The simulated shear catalogs in this test do not include shape noise to increase statistical power. In each panel we list the χ^2 of the ratio relative to one and the best fit amplitude. The errorbars represent the standard deviation of the mean of the 10 AGORA patches.

509 A. Cross-correlation bandpower recovery

510 In Fig. 6, for each of the AGORA simulated CMB lens-
 511 ing reconstructions, we plot the ratio of the average re-
 512 covered $C_\ell^{\kappa\gamma}$ cross-spectra over the “true” cross-spectra.
 513 Here the recovered cross-spectra are measured from all
 514 10 of the AGORA realizations of simulated CMB lensing
 515 reconstructions and simulated DES shear catalogs (with-
 516 out shape noise, to increase sensitivity to potential bi-
 517 ases). The “true” cross-spectra are calculated from the
 518 noiseless full-sky AGORA lensing maps.

519 We find that using the Pol lensing maps (bottom row

520 of Fig. 6) we are able to recover the cross-correlation
 521 bandpowers without bias, confirming that they are im-
 522 mune to foreground contamination and that our measure-
 523 ment pipeline correctly recovers the input power spectra.
 524 On the other hand, we find significant evidence for fore-
 525 ground biases in the GMV maps (top row of Fig. 6). On
 526 large to intermediate angular scales, this manifests as a
 527 negative $\sim 20 - 40\%$ bias, while on small angular scales
 528 ($\ell > 2000$) it becomes a large positive $\sim 50\%$ bias. The
 529 shape of this bias is qualitatively consistent with what is
 530 expected from tSZ contamination [45, 83].

531 For the Prof and MH lensing maps, which mainly at-
 532 tempt to remove tSZ contamination, we find hints of

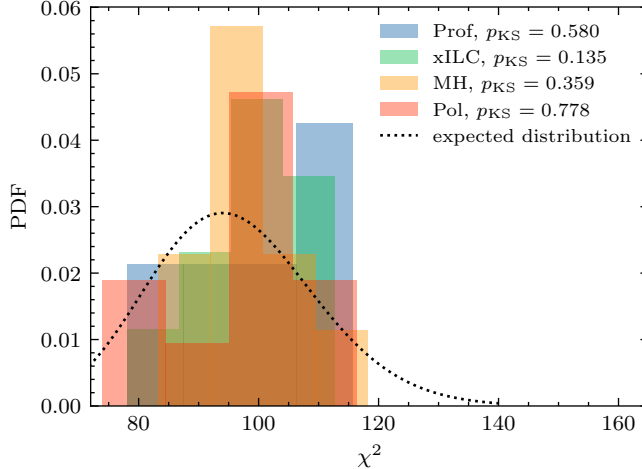


FIG. 7. Distributions of χ^2 values for each of the simulated SPT-3G x DES Y3 data vectors. For each variant we list the p -value corresponding to the null hypothesis that the values follow the expected distribution computed using a two-sided Kolmogorov-Smirnov test.

533 small (no more than a few percent) biases, potentially
 534 indicating either imperfect removal or potential CIB con-
 535 tamination. The xILC maps, which attempt to remove
 536 both tSZ and CIB contamination, are fairly consistent
 537 with no bias. AO: speculate about amounts of bias in
 538 different reconstructions: Prof and MH variants mainly
 539 remove tSZ, xILC might be better at removing both tSZ
 540 and CIB? AO: also comment on why we don't need to
 541 correct for a different QE response in the xcorr compared
 542 to the lensing auto

543

B. χ^2 test

544 In addition to confirming that the cross-correlation
 545 bandpowers are unbiased, we test our estimate of the
 546 covariance matrix by computing the distribution of $\chi^2 =$
 547 $\mathbf{d}^T \mathbf{C}^{-1} \mathbf{d}$ values for each set of simulated bandpowers.
 548 Under the assumption that the bandpowers are drawn
 549 from a multivariate Gaussian distribution, the χ^2 values
 550 are expected to follow a χ^2 -distribution with number of
 551 degrees of freedom equal to the length of the data vector.
 552 If our analytic estimate of the covariance matrix is incor-
 553 rect, then we would expect deviations from the expected
 554 distribution.

555 The results of this test are shown in Fig. 7 where we
 556 also list the p -values corresponding to the null hypothesis
 557 that the values follow the expected distribution computed
 558 using a two-sided Kolmogorov-Smirnov (KS) test. While
 559 this test is not particularly powerful due to the limited
 560 number of AGORA realizations, we do not find any ev-
 561 idence that the observed distributions deviate from the
 562 expected one for any of the non-GMV cross-correlations.
 563 Since the GMV data vectors are clearly biased due to
 564 foregrounds, we do not include their χ^2 values (which

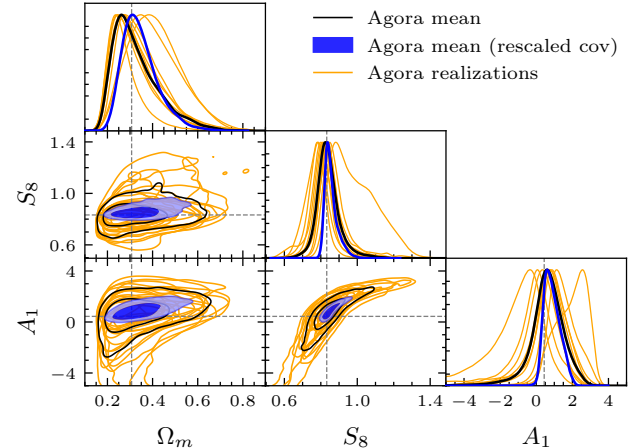


FIG. 8. AGORA parameter recovery test for the Pol $\kappa\gamma$ data vectors. We plot the marginal posterior distributions corresponding to the mean AGORA datavector with the data covariance in black and with the data covariance scaled by a factor of 1/10 in blue. The posteriors for each of the individual realizations are shown in orange.

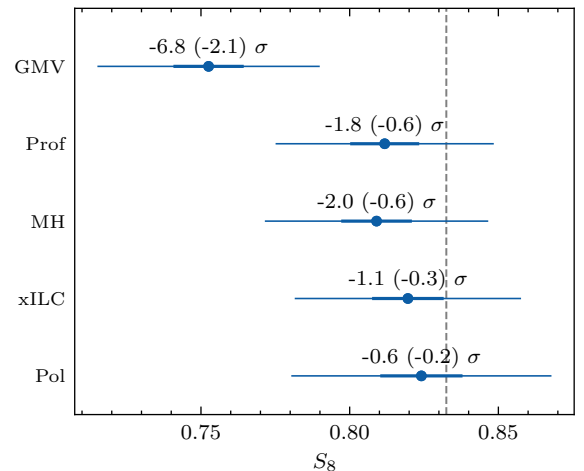


FIG. 9. AGORA S_8 recovery test for each of the five lensing map variants. The thick errorbars represent the marginalized errorbar on S_8 from the combination of all 10 realizations, while the thin errorbars are scaled by a factor of $\sqrt{10}$ to represent the mean errorbar of a single realization. We also list the resulting biases relative to the input value for the combined and (single realization) cases.

565 are generally biased $\sim 20\%$ high relative to the other
 566 variants) in Fig. 7.

C. Parameter recovery

567 When inferring cosmological parameters from the sim-
 568 ulated bandpowers, we use a slightly modified COSMOSIS
 569 pipeline compared to what is used on the data. 1. To
 570

be consistent with the MDPL2 cosmology, neutrinos are assumed to be massless. 2. The nonlinear matter power spectrum is computed using HMCode without baryonic feedback, since AGORA is based on a gravity-only N -body simulation.

We run the inference pipeline on all 10 AGORA realizations for each of the 5 lensing map variants. We also run the pipeline on the mean data vector for each lensing map variant with a covariance corresponding to a single realization and with a covariance that has been scaled by a factor of 1/10, representing the variance of the mean.

We show the results of this test on the Pol $\kappa\gamma$ data vectors in Fig. 8, where we plot the marginalized posteriors in the Ω_m - S_8 - A_1 parameter space. We find that the contours for individual realizations scatter around the true input values and the contours corresponding to the mean data vectors are correctly centered on the input values.

In Fig. 9 we summarize the marginalized constraints on S_8 obtained from each of the lensing map variants. Specifically, the thick errorbars represent the combined constraint obtained from all 10 realizations, while the thin errorbars are scaled by a factor of $\sqrt{10}$ to represent the mean errorbar of a single realization. When using the GMV reconstruction, we find a -6.8σ bias on S_8 when combining all 10 AGORA realizations, translating to roughly an average of a -2.1σ bias for a single realization. All of the other estimators result in constraints that are consistent with the input. Only the Prof/MH estimators can be considered to result in a slight tension with the input at roughly $1.8/2.0\sigma$ respectively when combining all 10 AGORA realizations.

VII. RESULTS

A. Detection significance

In Table IV we list the estimated signal-to-noise ratio for each set of cross-correlation bandpowers which we define as

$$\text{SNR} = \sqrt{\mathbf{d}^T \mathbf{C}^{-1} \mathbf{d} - N_d}, \quad (17)$$

where N_d is the length of the data vector. We also list the amplitude of the measured cross-correlations relative to the prediction assuming a *Planck* 2018 cosmology. This amplitude is calculated as

$$A_{\text{Planck}} = \frac{\mathbf{t}^T \mathbf{C}^{-1} \mathbf{d}}{\mathbf{t}^T \mathbf{C}^{-1} \mathbf{t}}, \quad (18)$$

where \mathbf{t} is the theory vector calculated using the fiducial model listed in Table II.

For all data combinations, we get high significance ($> 12\sigma$) detections of the $\kappa\gamma$ cross-correlation. The highest significance detection (15.5σ) is obtained when using the full shear sample and the profile-hardened lensing estimator. It is notable that when using the polarization-only estimator, we only lose ~ 2 points of SNR, indica-

Data vector	SNR	A_{Planck}
Full x GMV	13.9	0.86 ± 0.060
Full x Prof	15.5	0.98 ± 0.062
Full x MH	15.2	0.98 ± 0.063
Full x xILC	14.9	0.99 ± 0.065
Full x Pol	13.4	0.99 ± 0.075
Blue x Pol	12.8	1.08 ± 0.086

TABLE IV. Singal-to-noise ratios (SNR) and amplitudes relative to the Planck prediction (A_{Planck}) for each of the cross-correlation variants.

tive of the very low polarization noise levels in the SPT-3G maps. Right away, we can also see evidence of foreground biases in the GMV reconstruction. While the GMV reconstruction is expected to produce the highest SNR measurement, it is in fact 1.6 SNR points lower than the profile-hardened reconstruction due to the foreground bias that is expected to be negative across almost all scales. Additionally, the cross-correlation with the GMV reconstruction is the only one that is biased by more than 1σ relative to the *Planck* prediction. For all other variants we obtain values of A_{Planck} that are fully consistent with 1.

B. Cosmological constraints

Our main results are shown in Fig. 10 where we show the marginalized posteriors in the Ω_m - σ_8 - S_8 parameter space obtained from the Full x Pol and Blue x Pol data vectors. We also compare our results with those from three external data sets: DES Y3 + KiDS-1000 cosmic shear [4], DES Y3 blue shear [22], and measurements of the primary CMB from *Planck* (TTTEEE+lowE) [23]. While they are significantly less constraining, we find that our constraints using both the Full x Pol and the Blue x Pol data vectors are fully consistent with both shear-only and primary CMB results.

Using the Full x Pol data vector and assuming the NLA model for galaxy IA, we obtain:

$$\begin{aligned} \Omega_m &= 0.288^{+0.034}_{-0.094}, \\ S_8 &= 0.829^{+0.050}_{-0.064}. \end{aligned}$$

Using the Blue x Pol data vector and assuming no IA, we obtain:

$$\begin{aligned} \Omega_m &= 0.312^{+0.039}_{-0.10}, \\ S_8 &= 0.853 \pm 0.032. \end{aligned}$$

We summarize the the main cosmological constraints from all considered data combinations in Table V. For the parameters Ω_m and S_8 , we list the marginalized 68% confidence intervals and the estimated MAP points. We also list the χ^2 value of the estimated MAP point.

We summarize the results from several analysis variations in the following subsections and in Fig. 11.

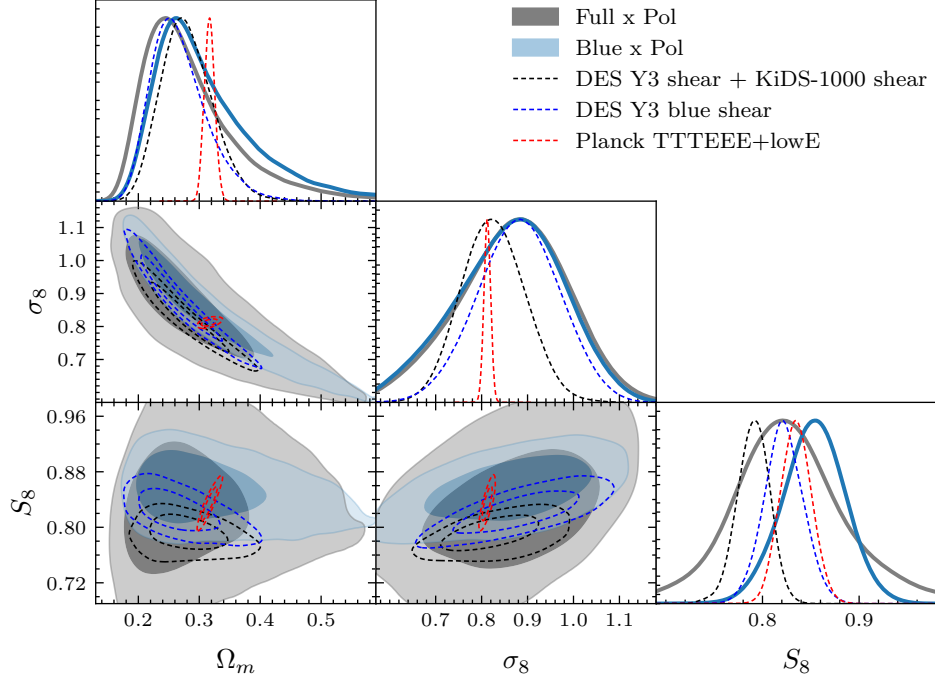


FIG. 10. Marginalized posteriors in the Ω_m - σ_8 - S_8 parameter space for our Full x Pol and Blue x Pol data vectors. We also compare our results with published cosmic shear constraints (DES Y3 + KiDS-1000 [4] and DES Y3 blue shear [22]) and the primary CMB (*Planck* TTTEEEE+lowE [23]).

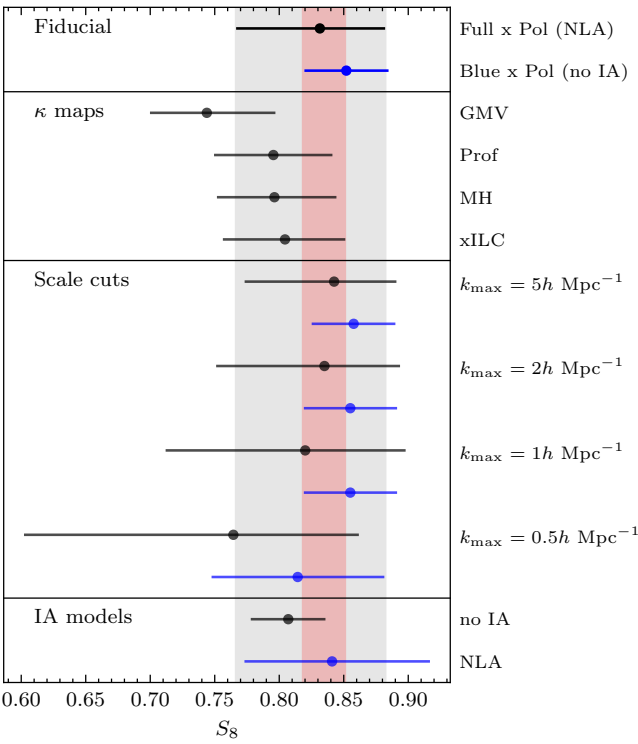


FIG. 11. Effect of different analysis choices on the resulting S_8 constraint. The vertical red band corresponds to the constraint from *Planck*TTTEEEE+lowE.

Data vector	S_8	$\chi^2_{\text{MAP}} / \text{PTE}$
Full x GMV	$0.744^{+0.053}_{-0.044}$ (0.79)	84.9 / 0.71
Full x Prof	0.795 ± 0.052 (0.82)	87.0 / 0.65
Full x MH	0.796 ± 0.052 (0.83)	83.1 / 0.75
Full x xILC	0.804 ± 0.054 (0.84)	83.8 / 0.74
Full x Pol	$0.831^{+0.051}_{-0.065}$ (0.85)	98.3 / 0.33
Blue x Pol	0.852 ± 0.033 (0.88)	101.2 / 0.29

TABLE V. Summary of S_8 constraints for all data combinations considered. For each combination we list the marginalized 68% confidence limits as well as the maximum a posteriori (MAP) values in parentheses. We also list the χ^2 value at the estimated MAP point and the estimated probability-to-exceed (PTE) value calculated using the number of degrees of freedom as described in Section V B 2. The effective number of constrained parameters for each data combination is 3.2, 3.2, 3.3, 3.2, 3.1, and 2.0 respectively.

1. CMB lensing foregrounds

In the second section of Fig. 11 we compare the constraints obtained when cross-correlating all five variants of the CMB lensing maps with the full DES Y3 sample. Generally, we see very good agreement between all of the data combinations, except for the one that uses the GMV map which is clearly biased towards lower S_8 values, consistent with the lower amplitude found relative to *Planck*

(Table IV) compared to the other data combinations. We find that the signs of foregrounds in the data are fairly consistent with the AGORA foreground models. Using TENSIOMETER to calculate the Gaussian tension between marginalized S_8 posteriors, we find differences of 1.7 σ , 0.7 σ , 0.7 σ , 0.5 σ , and 0.1 σ between *Planck* TT-TEEE+lowE and the GMV, Prof, MH, xILC, and Pol $\kappa\gamma$ cross-correlations respectively. These differences are very similar to the average AGORA single-realization biases (Fig. 9).

Notably, while the Full x Pol data vector has about 16% less total SNR compared to the Full x Prof data vector, the constraint on S_8 is only 12% wider.

675

2. Scale cuts

A potential concern about this analysis is that we attempt to use all scales to extract cosmological constraints while using relatively simplistic models for IA and baryonic feedback. Since the measured $\kappa\gamma$ cross-correlation on its own is unable to constrain the parameters related to these effects, we conclude that there is not enough sensitivity in the data on small scales to warrant more complicated models. For completeness, in the third section of Fig. 11 we show the marginalized constraints on S_8 obtained when applying scale cuts of $k_{\max} = 5, 2, 1$, and $0.5h \text{ Mpc}^{-1}$ as described in Section VB3. As expected, applying more conservative scale cuts significantly loosens the S_8 constraint, but we do not see any significant shifts in the mean values that might indicate biases due to mis-modelling of small scales.

691

3. Intrinsic alignments

By comparing our results obtained using the Full x Pol combination and the Blue x Pol combination, we find that they are robust against unmodelled IA systematics.

Even though the Blue x Pol combination has the lowest SNR, we are able to obtain the tightest S_8 constraint from this combination. This is simply due to the fact that we assume zero IA amplitude for the blue sample, breaking the degeneracy between S_8 and IA. Together with [22], this highlights the usefulness of mitigating IA at the sample selection level.

702

C. Combining with Planck

We run a joint analysis of our measured $\kappa\gamma$ cross-correlation with the *Planck* 2018 TTTEEE+lowE likelihood. This has the effect of putting a tight prior on the cosmological parameters, allowing us to put constraints on astrophysical parameters (IA and baryonic feedback).

Fig. 12 shows the marginalized posteriors resulting from the combination of the Pol and Prof cross-correlations with *Planck*. By combining with *Planck*, we

are able to significantly tighten the constraints on the IA amplitude of the DES Y3 sample. From the Pol cross-correlation alone, we find $A_1 = 0.32^{+1.0}_{-0.76}$, while in combination with *Planck* we find $A_1 = 0.48 \pm 0.45$. We get a very similar constraint using the Prof cross-correlation combined with *Planck*: $A_1 = 0.39 \pm 0.41$. In all cases, we see no evidence for any redshift evolution of the IA amplitude. It is noteworthy that these constraints on the IA amplitude are fully consistent with (and in some cases tighter than) the constraints found in shear auto-correlation analyses [4, 49, 66].

By combining with *Planck*, we can also test our assumption of no IA in the DES blue sample. When analyzing Blue x Pol + *Planck* assuming NLA, we find an IA amplitude of $A_1 = -0.23^{+0.55}_{-0.47}$, consistent with zero and the constraint found by [22].

Finally, we find that our data have some mild sensitivity to the strength of baryonic feedback as parameterized by $\log T_{\text{AGN}}$. The Pol lensing maps are too noisy on small scales to provide constraining power on the strength of baryonic feedback, even when mitigating IA using the blue sample selection. By combining the Full x Prof cross-correlation with *Planck*, we begin to see evidence for small-scale suppression of the matter power spectrum from baryonic feedback. We get a 68% credible lower limit of $\log T_{\text{AGN}} > 7.70$ which is consistent with the amount of suppression generally found in shear auto-correlation analyses [11].

VIII. CONCLUSIONS

The cross-correlation between CMB lensing (κ) and cosmic shear (γ) provides a useful consistency test that is less sensitive to the measurement systematics of each survey. We have measured the cross-correlation between CMB lensing from SPT-3G and DES Y3 cosmic shear over an overlapping sky area of approximately 1,300 deg².

The main findings of this analysis are as follows.

- We detect the $\kappa\gamma$ cross-correlation at a significance of 13 σ when only using CMB polarization data in the lensing reconstruction. The significance increases to $\sim 15 - 16\sigma$ when including temperature data and using some foreground mitigation technique.
- We fit a model to the data, marginalizing over galaxy intrinsic alignments, baryonic feedback, and cosmic shear nuisance parameters, and find a 7% constraint on the amplitude of matter clustering S_8 that is consistent with both results from *Planck* and from cosmic shear surveys.
- Using a high-purity sub-selection of blue star-forming galaxies from the full DES Y3 catalog that is expected to be less impacted by IA than the full sample [22, 84], we show that reducing the uncertainty on the IA amplitude, significantly improves

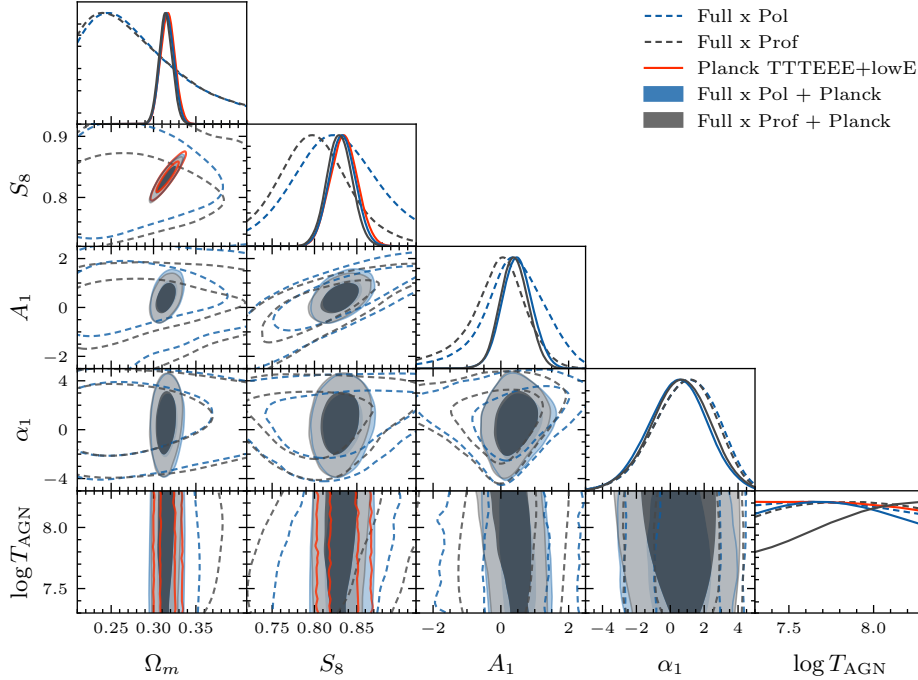


FIG. 12. Cosmological and astrophysical constraints from the combination of *Planck* with the Pol and Prof $\kappa\gamma$ cross-correlations.

the constraining power on S_8 . When modeling the $\kappa\gamma$ cross-correlation with the blue sample under the assumption of no IA, we obtain a 4% constraint on S_8 that is still consistent with both the primary CMB and cosmic shear surveys.

- We use the *Planck* 2018 results to put a tight prior on cosmological parameters and show that the measured $\kappa\gamma$ cross-correlation has some sensitivity to small-scale physics. Using the Pol x Full data vector, we find a 1.1σ constraint on the IA amplitude that is comparable to what is found in the full DES Y3 cosmic shear analysis. We find no evidence for significant redshift evolution of this amplitude. Using the Prof x Full data vector, we additionally find hints of a small-scale suppression of power due to baryonic feedback.

These results represent the first high-significance detection of the $\kappa\gamma$ cross-correlation using a polarization-only lensing reconstruction and are a significant improvement over the first such measurement with POLAR-BEAR and HSC [14]. This highlights the power of polarization-only CMB lensing reconstructions to mitigate extragalactic foregrounds when very low noise CMB polarization observations are available.

Future work: include shear autos to measure the small scale matter power spectrum, work towards 6x2-pt analysis

With data from future surveys, more work will need to be done to ensure accurate modelling on small scales. In

particular, IA modeling will need significant attention. [perturbative and non-perturbative techniques]

ACKNOWLEDGMENTS

The South Pole Telescope program is supported by the National Science Foundation (NSF) through awards OPP-1852617 and OPP-2332483. Partial support is also provided by the Kavli Institute of Cosmological Physics at the University of Chicago. Argonne National Laboratory's work was supported by the U.S. Department of Energy, Office of High Energy Physics, under contract DE-AC02-06CH11357. The UC Davis group acknowledges support from Michael and Ester Vaida. Work at the Fermi National Accelerator Laboratory (Fermilab), a U.S. Department of Energy, Office of Science, Office of High Energy Physics HEP User Facility, is managed by Fermi Forward Discovery Group, LLC, acting under Contract No. 89243024CSC000002. The Melbourne authors acknowledge support from the Australian Research Council's Discovery Project scheme (No. DP210102386). The Paris group has received funding from the European Research Council (ERC) under the European Union's Horizon 2020 research and innovation program (grant agreement No 101001897), and funding from the Centre National d'Etudes Spatiales. The SLAC group is supported in part by the Department of Energy at SLAC National Accelerator Laboratory, under contract DE-AC02-76SF00515. This work was partially supported by the Center for AstroPhysical Surveys (CAPS) at the Na-

tional Center for Supercomputing Applications (NCSA), University of Illinois Urbana-Champaign. This work made use of the following computing resources: the Illinois Campus Cluster, a computing resource that is operated by the Illinois Campus Cluster Program (ICCP) in conjunction with the National Center for Supercomputing Applications (NCSA) and which is supported by funds from the University of Illinois Urbana-Champaign; and Crossover, a high-performance computing cluster operated by the Laboratory Computing Resource Center at Argonne National Laboratory. This work relied on NUMPY [85] and SCIPY [86] for numerical calculations, MATPLOTLIB [87] for plotting, and GETDIST [88] for plotting and analyzing posterior distributions.

845

835 Appendix A: Additional validation test plots

In Fig. 13 we show the measured B -mode cross-correlations when using the Pol lensing reconstruction

838 and both of the DES shear samples. We find no significant evidence for non-zero B -modes. Out of all of the
 839 data vectors (including the GMV, Prof, MH, and xILC
 840 lensing reconstructions), the worst χ^2 value is 37.6 with
 841 24 degrees of freedom for bin 2 of the full shear sample.
 842 While this is somewhat high, it is within the expected dis-
 843 tribution when considering four independent shear bins.

844

Appendix B: Full posteriors

846 For completeness, we show the full posteriors for the
 847 Full x Pol, Full x Prof, and Blue x Pol data combinations
 848 in Fig. 14.

- 849 [1] Bartelmann, M., & Schneider, P. Weak gravitational 886 sistent Structure Growth Measurements from Joint ACT,
 850 lensing. 2001, Phys. Rep., 340, 291, doi: [10.1016/S0370-1573\(00\)00082-X](https://doi.org/10.1016/S0370-1573(00)00082-X) 887 SPT, and Planck CMB Lensing. 2026, Phys. Rev. Lett.,
 851 136, 021001, doi: [10.1103/k5yr-3h6d](https://doi.org/10.1103/k5yr-3h6d)
- 852 [2] Kilbinger, M. Cosmology with cosmic shear observa- 888 tions: a review. 2015, Reports on Progress in Physics, 889 78, 086901, doi: [10.1088/0034-4885/78/8/086901](https://doi.org/10.1088/0034-4885/78/8/086901)
- 853 [3] Abbott, T. M. C., Aguena, M., Alarcon, A., et al. 890 Dark Energy Survey Year 3 results: Cosmological con- 891 straints from galaxy clustering and weak lensing. 2022, 892 Phys. Rev. D, 105, 023520, doi: [10.1103/PhysRevD.105.023520](https://doi.org/10.1103/PhysRevD.105.023520)
- 854 [4] Dark Energy Survey and Kilo-Degree Survey Collabo- 893 ration, Abbott, T. M. C., Aguena, M., et al. DES Y3 + 894 KiDS-1000: Consistent cosmology combining cosmic 895 shear surveys. 2023, The Open Journal of Astrophysics, 896 6, 36, doi: [10.21105/astro.2305.17173](https://doi.org/10.21105/astro.2305.17173)
- 855 [5] Wright, A. H., Stölzner, B., Asgari, M., et al. KiDS- 897 Legacy: Cosmological constraints from cosmic shear with 898 the complete Kilo-Degree Survey. 2025, A&A, 703, A158, 899 doi: [10.1051/0004-6361/202554908](https://doi.org/10.1051/0004-6361/202554908)
- 860 [6] Dalal, R., Li, X., Nicola, A., et al. Hyper Suprime- 900 Cam Year 3 results: Cosmology from cosmic shear power 901 spectra. 2023, Phys. Rev. D, 108, 123519, doi: [10.1103/PhysRevD.108.123519](https://doi.org/10.1103/PhysRevD.108.123519)
- 861 [7] Carron, J., Mirmelstein, M., & Lewis, A. CMB lensing 902 from Planck PR4 maps. 2022, J. Cosmology Astropart. 903 Phys., 2022, 039, doi: [10.1088/1475-7516/2022/09/039](https://doi.org/10.1088/1475-7516/2022/09/039)
- 862 [8] Madhavacheril, M. S., Qu, F. J., Sherwin, B. D., et al. 904 The Atacama Cosmology Telescope: DR6 Gravitational 905 Lensing Map and Cosmological Parameters. 2024, ApJ, 906 962, 113, doi: [10.3847/1538-4357/acff5f](https://doi.org/10.3847/1538-4357/acff5f)
- 863 [9] Ge, F., Millea, M., Camphus, E., et al. Cosmol- 907 ogy from CMB lensing and delensed EE power spec- 908 tra using 2019–2020 SPT-3G polarization data. 2025, 909 Phys. Rev. D, 111, 083534, doi: [10.1103/PhysRevD.111.083534](https://doi.org/10.1103/PhysRevD.111.083534)
- 864 [10] Qu, F. J., Ge, F., Wu, W. L. K., et al. Unified and Con- 910
- 865 [11] Amon, A., & Efstathiou, G. A non-linear solution to 911 the S_8 tension? 2022, MNRAS, 516, 5355, doi: [10.1093/mnras/stac2429](https://doi.org/10.1093/mnras/stac2429)
- 866 [12] Preston, C., Amon, A., & Efstathiou, G. A non-linear 912 solution to the S_8 tension - II. Analysis of DES Year 3 913 cosmic shear. 2023, MNRAS, 525, 5554, doi: [10.1093/mnras/stad2573](https://doi.org/10.1093/mnras/stad2573)
- 867 [13] Osborne, S. J., Hanson, D., & Doré, O. Extragalactic 914 foreground contamination in temperature-based CMB 915 lens reconstruction. 2014, J. Cosmology Astropart. Phys., 916 2014, 024, doi: [10.1088/1475-7516/2014/03/024](https://doi.org/10.1088/1475-7516/2014/03/024)
- 868 [14] Namikawa, T., Chinone, Y., Miyatake, H., et al. Ev- 917 idence for the Cross-correlation between Cosmic Mi- 918 crowave Background Polarization Lensing from Polar- 919 bear and Cosmic Shear from Subaru Hyper Suprime- 920 Cam. 2019, ApJ, 882, 62, doi: [10.3847/1538-4357/ab3424](https://doi.org/10.3847/1538-4357/ab3424)
- 869 [15] Marques, G. A., Liu, J., Huffenberger, K. M., & 921 Colin Hill, J. Cross-correlation between Subaru Hyper 922 Suprime-Cam Galaxy Weak Lensing and Planck Cosmic 923 Microwave Background Lensing. 2020, ApJ, 904, 182, 924 doi: [10.3847/1538-4357/abc003](https://doi.org/10.3847/1538-4357/abc003)
- 870 [16] Robertson, N. C., Alonso, D., Harnois-Déraps, J., et al. 925 Strong detection of the CMB lensing and galaxy weak 926 lensing cross-correlation from ACT-DR4, Planck Legacy, 927 and KiDS-1000. 2021, A&A, 649, A146, doi: [10.1051/0004-6361/202039975](https://doi.org/10.1051/0004-6361/202039975)
- 871 [17] Shaikh, S., Harrison, I., van Engelen, A., et al. Cos- 928 mology from cross-correlation of ACT-DR4 CMB lens- 929 ing and DES-Y3 cosmic shear. 2024, MNRAS, 528, 2112, 930 doi: [10.1093/mnras/stad3987](https://doi.org/10.1093/mnras/stad3987)
- 872 [18] Omori, Y., Baxter, E. J., Chang, C., et al. Joint analysis 931 of Dark Energy Survey Year 3 data and CMB lensing 932 from SPT and Planck. I. Construction of CMB lensing 933

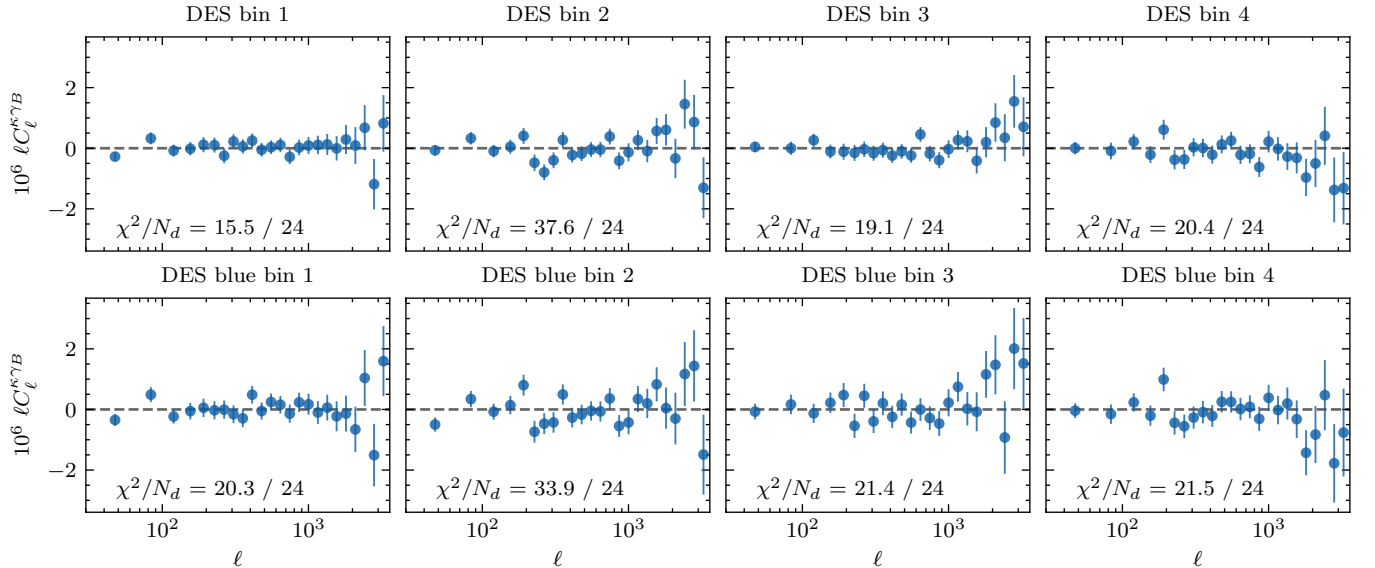


FIG. 13. Top row: B -mode $\kappa\gamma$ cross-correlations for the full shear sample and the Pol lensing reconstruction. Bottom row: same as top row, but for the blue shear subsample. We list the χ^2 values for each data vector relative to zero.

- maps and modeling choices. 2023, Phys. Rev. D, 107, 023529, doi: [10.1103/PhysRevD.107.023529](https://doi.org/10.1103/PhysRevD.107.023529)
- [19] Chang, C., Omori, Y., Baxter, E. J., et al. Joint analysis of Dark Energy Survey Year 3 data and CMB lensing from SPT and Planck. II. Cross-correlation measurements and cosmological constraints. 2023, Phys. Rev. D, 107, 023530, doi: [10.1103/PhysRevD.107.023530](https://doi.org/10.1103/PhysRevD.107.023530)
- [20] Abbott, T. M. C., Aguena, M., Alarcon, A., et al. Joint analysis of Dark Energy Survey Year 3 data and CMB lensing from SPT and Planck. III. Combined cosmological constraints. 2023, Phys. Rev. D, 107, 023531, doi: [10.1103/PhysRevD.107.023531](https://doi.org/10.1103/PhysRevD.107.023531)
- [21] Omori, Y., & et al. Curved-sky lensing reconstruction using the 2019-2020 data from the SPT-3G instrument. in prep.
- [22] McCullough, J., Amon, A., Legnani, E., et al. Dark Energy Survey Year 3: Blue Shear. 2024, arXiv e-prints, arXiv:2410.22272, doi: [10.48550/arXiv.2410.22272](https://doi.org/10.48550/arXiv.2410.22272)
- [23] Planck Collaboration, Aghanim, N., Akrami, Y., et al. Planck 2018 results. VI. Cosmological parameters. 2020, A&A, 641, A6, doi: [10.1051/0004-6361/201833910](https://doi.org/10.1051/0004-6361/201833910)
- [24] Benson, B. A., Ade, P. A. R., Ahmed, Z., et al. SPT-3G: a next-generation cosmic microwave background polarization experiment on the South Pole telescope. 2014, in Society of Photo-Optical Instrumentation Engineers (SPIE) Conference Series, Vol. 9153, Millimeter, Submillimeter, and Far-Infrared Detectors and Instrumentation for Astronomy VII, ed. W. S. Holland & J. Zmuidzinas, 91531P, doi: [10.1117/12.2057305](https://doi.org/10.1117/12.2057305)
- [25] Carlstrom, J. E., Ade, P. A. R., Aird, K. A., et al. The 10 Meter South Pole Telescope. 2011, PASP, 123, 568, doi: [10.1086/659879](https://doi.org/10.1086/659879)
- [26] Camphuis, E., Quan, W., Balkenhol, L., et al. SPT-3G D1: CMB temperature and polarization power spectra and cosmology from 2019 and 2020 observations of the SPT-3G Main field. 2025, arXiv e-prints, arXiv:2506.20707, doi: [10.48550/arXiv.2506.20707](https://doi.org/10.48550/arXiv.2506.20707)
- [27] Okamoto, T., & Hu, W. Cosmic microwave background lensing reconstruction on the full sky. 2003, Phys. Rev. D, 67, 083002, doi: [10.1103/PhysRevD.67.083002](https://doi.org/10.1103/PhysRevD.67.083002)
- [28] Maniyar, A. S., Ali-Haïmoud, Y., Carron, J., Lewis, A., & Madhavacheril, M. S. Quadratic estimators for CMB weak lensing. 2021, Phys. Rev. D, 103, 083524, doi: [10.1103/PhysRevD.103.083524](https://doi.org/10.1103/PhysRevD.103.083524)
- [29] Smith, K. M., Cooray, A., Das, S., Doré, O., Hanson, D., Hirata, C., Kaplinghat, M., Keating, B., Loverde, M., Miller, N., Rocha, G., Shimon, M., & Zahn, O. Gravitational Lensing. 2009, in American Institute of Physics Conference Series, Vol. 1141, CMB Polarization Workshop: Theory and Foregrounds: CMBPol Mission Concept Study, ed. S. Dodelson, D. Baumann, A. Cooray, J. Dunkley, A. Fraisse, M. G. Jackson, A. Kogut, L. Krauss, M. Zaldarriaga, & K. Smith (AIP), 121–178, doi: [10.1063/1.3160886](https://doi.org/10.1063/1.3160886)
- [30] Deutsch, A.-S., Johnson, M. C., Münchmeyer, M., & Terrana, A. Polarized Sunyaev Zel'dovich tomography. 2018, J. Cosmology Astropart. Phys., 2018, 034, doi: [10.1088/1475-7516/2018/04/034](https://doi.org/10.1088/1475-7516/2018/04/034)
- [31] Feng, C., & Holder, G. Polarization of the Cosmic Infrared Background Fluctuations. 2020, ApJ, 897, 140, doi: [10.3847/1538-4357/ab9013](https://doi.org/10.3847/1538-4357/ab9013)
- [32] Namikawa, T., Hanson, D., & Takahashi, R. Bias-hardened CMB lensing. 2013, MNRAS, 431, 609, doi: [10.1093/mnras/stt195](https://doi.org/10.1093/mnras/stt195)
- [33] Madhavacheril, M. S., & Hill, J. C. Mitigating foreground biases in CMB lensing reconstruction using cleaned gradients. 2018, Phys. Rev. D, 98, 023534, doi: [10.1103/PhysRevD.98.023534](https://doi.org/10.1103/PhysRevD.98.023534)
- [34] Raghunathan, S., & Omori, Y. A Cross-internal Linear Combination Approach to Probe the Secondary CMB Anisotropies: Kinematic Sunyaev-Zel'dovich Effect and CMB Lensing. 2023, ApJ, 954, 83, doi: [10.3847/1538-4357/ace0c6](https://doi.org/10.3847/1538-4357/ace0c6)
- [35] Nakato, Y., Kimmy Wu, W. L., Silva Oliveira, A. C., Omori, Y., & Maniyar, A. S. Foreground Mitigation for CMB Lensing with the Global Minimum

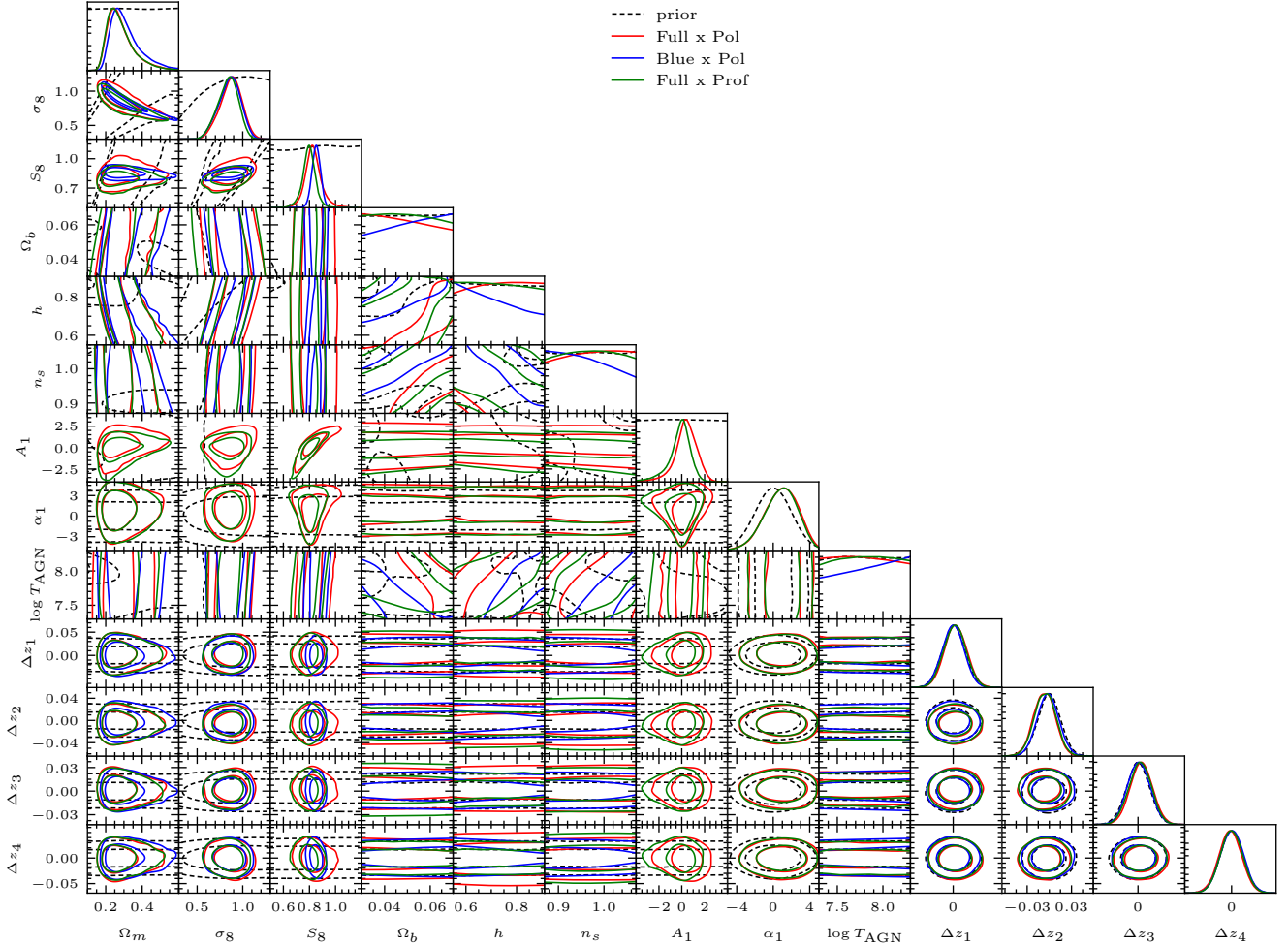


FIG. 14. Full posteriors for the Full x Pol, Blue x Pol, and Full x Prof $\kappa\gamma$ cross-correlations. The black dashed contours show the result of sampling the prior as specified in Table II.

- 999 Variance Quadratic Estimator. 2025, arXiv e-prints, 1021
1000 arXiv:2512.08908, doi: [10.48550/arXiv.2512.08908](https://doi.org/10.48550/arXiv.2512.08908) 1022
1001 [36] The Dark Energy Survey Collaboration. The Dark En- 1023
1002 ergy Survey. 2005, arXiv e-prints, astro, doi: [10.48550/arXiv.astro-ph/0510346](https://doi.org/10.48550/arXiv.astro-ph/0510346) 1024
1003 [37] Abbott, T. M. C., Abdalla, F. B., Allam, S., et al. The 1025
1004 Dark Energy Survey: Data Release 1. 2018, ApJS, 239, 1026
1005 18, doi: [10.3847/1538-4365/aae9f0](https://doi.org/10.3847/1538-4365/aae9f0) 1027
1006 [38] Abbott, T. M. C., Adamów, M., Aguena, M., et al. The 1028
1007 Dark Energy Survey Data Release 2. 2021, ApJS, 255, 1029
1008 20, doi: [10.3847/1538-4365/ac00b3](https://doi.org/10.3847/1538-4365/ac00b3) 1030
1009 [39] Flaugher, B., Diehl, H. T., Honscheid, K., et al. The 1031
1010 Dark Energy Camera. 2015, AJ, 150, 150, doi: [10.1088/0004-6256/150/5/150](https://doi.org/10.1088/0004-6256/150/5/150) 1032
1011 [40] Sevilla-Noarbe, I., Bechtol, K., Carrasco Kind, M., et al. 1033
1012 Dark Energy Survey Year 3 Results: Photometric Data 1034
1013 Set for Cosmology. 2021, ApJS, 254, 24, doi: [10.3847/1538-4365/abeb66](https://doi.org/10.3847/1538-4365/abeb66) 1035
1014 [41] Gatti, M., Sheldon, E., Amon, A., et al. Dark energy 1036
1015 survey year 3 results: weak lensing shape catalogue. 2021, 1037
1016 MNRAS, 504, 4312, doi: [10.1093/mnras/stab918](https://doi.org/10.1093/mnras/stab918) 1038
1017 [42] Myles, J., Alarcon, A., Amon, A., et al. Dark En- 1039
1018 ergy Survey Year 3 results: redshift calibration of the 1040
1019 weak lensing source galaxies. 2021, MNRAS, 505, 4249, 1041
1020 doi: [10.1093/mnras/stab1515](https://doi.org/10.1093/mnras/stab1515)
1021 [43] Sheldon, E. S., & Huff, E. M. Practical Weak-lensing 1022
1022 Shear Measurement with Metacalibration. 2017, ApJ, 841, 24, doi: [10.3847/1538-4357/aa704b](https://doi.org/10.3847/1538-4357/aa704b)
1023 Huff, E., & Mandelbaum, R. Metacalibration: Direct 1024
1024 Self-Calibration of Biases in Shear Measurement. 2017, 1025
1025 arXiv e-prints, arXiv:1702.02600, doi: [10.48550/arXiv.1702.02600](https://doi.org/10.48550/arXiv.1702.02600)
1026 [45] Omori, Y. AGORA: Multicomponent simulation for 1027
1027 cross-survey science. 2024, MNRAS, 530, 5030, doi: [10.1093/mnras/stae1031](https://doi.org/10.1093/mnras/stae1031)
1028 [46] Klypin, A., Yepes, G., Gottlöber, S., Prada, F., & Heß, 1029
1029 S. MultiDark simulations: the story of dark matter halo 1030
1030 concentrations and density profiles. 2016, MNRAS, 457, 1031
1031 4340, doi: [10.1093/mnras/stw248](https://doi.org/10.1093/mnras/stw248)
1032 [47] Abbott, T. M. C., Abdalla, F. B., Alarcon, A., et al. 1033
1033 Dark Energy Survey year 1 results: Cosmological 1034
1034 constraints from galaxy clustering and weak lensing. 2018, 1035
1035 Phys. Rev. D, 98, 043526, doi: [10.1103/PhysRevD.98.043526](https://doi.org/10.1103/PhysRevD.98.043526)

- [48] Nicola, A., García-García, C., Alonso, D., Dunkley, J., Ferreira, P. G., Slosar, A., & Spergel, D. N. Cosmic shear power spectra in practice. 2021, *J. Cosmology Astropart. Phys.*, 2021, 067, doi: [10.1088/1475-7516/2021/03/067](https://doi.org/10.1088/1475-7516/2021/03/067)
- [49] Doux, C., Jain, B., Zeurcher, D., et al. Dark energy survey year 3 results: cosmological constraints from the analysis of cosmic shear in harmonic space. 2022, *MNRAS*, 515, 1942, doi: [10.1093/mnras/stac1826](https://doi.org/10.1093/mnras/stac1826)
- [50] Gorski, K. M., Hivon, E., Banday, A. J., Wandelt, B. D., Hansen, F. K., Reinecke, M., & Bartelmann, M. HEALPix: A Framework for High-Resolution Discretization and Fast Analysis of Data Distributed on the Sphere. 2005, *ApJ*, 622, 759, doi: [10.1086/427976](https://doi.org/10.1086/427976)
- [51] Zonca, A., Singer, L., Lenz, D., Reinecke, M., Rosset, C., Hivon, E., & Gorski, K. healpy: equal area pixelization and spherical harmonics transforms for data on the sphere in Python. 2019, *The Journal of Open Source Software*, 4, 1298, doi: [10.21105/joss.01298](https://doi.org/10.21105/joss.01298)
- [52] Zaldarriaga, M., & Seljak, U. All-sky analysis of polarization in the microwave background. 1997, *Phys. Rev. D*, 55, 1830, doi: [10.1103/PhysRevD.55.1830](https://doi.org/10.1103/PhysRevD.55.1830)
- [53] Alonso, D., Sanchez, J., Slosar, A., & LSST Dark Energy Science Collaboration. A unified pseudo- C_ℓ framework. 2019, *MNRAS*, 484, 4127, doi: [10.1093/mnras/stz093](https://doi.org/10.1093/mnras/stz093)
- [54] Hivon, E., Gorski, K. M., Netterfield, C. B., Crill, B. P., Prunet, S., & Hansen, F. MASTER of the Cosmic Microwave Background Anisotropy Power Spectrum: A Fast Method for Statistical Analysis of Large and Complex Cosmic Microwave Background Data Sets. 2002, *ApJ*, 567, 2, doi: [10.1086/338126](https://doi.org/10.1086/338126)
- [55] García-García, C., Alonso, D., & Bellini, E. Disconnected pseudo- C_ℓ covariances for projected large-scale structure data. 2019, *J. Cosmology Astropart. Phys.*, 2019, 043, doi: [10.1088/1475-7516/2019/11/043](https://doi.org/10.1088/1475-7516/2019/11/043)
- [56] Limber, D. N. The Analysis of Counts of the Extra-galactic Nebulae in Terms of a Fluctuating Density Field. 1953, *ApJ*, 117, 134, doi: [10.1086/145672](https://doi.org/10.1086/145672)
- [57] LoVerde, M., & Afshordi, N. Extended Limber approximation. 2008, *Phys. Rev. D*, 78, 123506, doi: [10.1103/PhysRevD.78.123506](https://doi.org/10.1103/PhysRevD.78.123506)
- [58] Lewis, A., Challinor, A., & Lasenby, A. Efficient Computation of Cosmic Microwave Background Anisotropies in Closed Friedmann-Robertson-Walker Models. 2000, *ApJ*, 538, 473, doi: [10.1086/309179](https://doi.org/10.1086/309179)
- [59] Lewis, A., & Challinor, A. 2011, CAMB: Code for Anisotropies in the Microwave Background, *Astrophysics Source Code Library*, record ascl:1102.026. <http://ascl.net/1102.026>
- [60] Mead, A. J., Brieden, S., Tröster, T., & Heymans, C. HMCODE-2020: improved modelling of non-linear cosmological power spectra with baryonic feedback. 2021, *MNRAS*, 502, 1401, doi: [10.1093/mnras/stab082](https://doi.org/10.1093/mnras/stab082)
- [61] Troxel, M. A., & Ishak, M. The intrinsic alignment of galaxies and its impact on weak gravitational lensing in an era of precision cosmology. 2015, *Phys. Rep.*, 558, 1, doi: [10.1016/j.physrep.2014.11.001](https://doi.org/10.1016/j.physrep.2014.11.001)
- [62] Lamman, C., Tsaprazi, E., Shi, J., Šarčević, N. N., Pyne, S., Legnani, E., & Ferreira, T. The IA Guide: A Breakdown of Intrinsic Alignment Formalisms. 2024, *The Open Journal of Astrophysics*, 7, 14, doi: [10.21105/astro.2309.08605](https://doi.org/10.21105/astro.2309.08605)
- [63] Blazek, J. A., MacCrann, N., Troxel, M. A., & Fang, X. Beyond linear galaxy alignments. 2019, *Phys. Rev. D*, 100, 103506, doi: [10.1103/PhysRevD.100.103506](https://doi.org/10.1103/PhysRevD.100.103506)
- [64] Hirata, C. M., & Seljak, U. Intrinsic alignment-lensing interference as a contaminant of cosmic shear. 2004, *Phys. Rev. D*, 70, 063526, doi: [10.1103/PhysRevD.70.063526](https://doi.org/10.1103/PhysRevD.70.063526)
- [65] Bridle, S., & King, L. Dark energy constraints from cosmic shear power spectra: impact of intrinsic alignments on photometric redshift requirements. 2007, *New Journal of Physics*, 9, 444, doi: [10.1088/1367-2630/9/12/444](https://doi.org/10.1088/1367-2630/9/12/444)
- [66] Secco, L. F., Samuroff, S., Krause, E., et al. Dark Energy Survey Year 3 results: Cosmology from cosmic shear and robustness to modeling uncertainty. 2022, *Phys. Rev. D*, 105, 023515, doi: [10.1103/PhysRevD.105.023515](https://doi.org/10.1103/PhysRevD.105.023515)
- [67] Chisari, N. E., Mead, A. J., Joudaki, S., Ferreira, P. G., Schneider, A., Mohr, J., Tröster, T., Alonso, D., McCarthy, I. G., Martin-Alvarez, S., Devriendt, J., Slyz, A., & van Daalen, M. P. Modelling baryonic feedback for survey cosmology. 2019, *The Open Journal of Astrophysics*, 2, 4, doi: [10.21105/astro.1905.06082](https://doi.org/10.21105/astro.1905.06082)
- [68] McCarthy, I. G., Schaye, J., Bird, S., & Le Brun, A. M. C. The BAHAMAS project: calibrated hydrodynamical simulations for large-scale structure cosmology. 2017, *MNRAS*, 465, 2936, doi: [10.1093/mnras/stw2792](https://doi.org/10.1093/mnras/stw2792)
- [69] Amon, A., Gruen, D., Troxel, M. A., et al. Dark Energy Survey Year 3 results: Cosmology from cosmic shear and robustness to data calibration. 2022, *Phys. Rev. D*, 105, 023514, doi: [10.1103/PhysRevD.105.023514](https://doi.org/10.1103/PhysRevD.105.023514)
- [70] Doux, C., Chang, C., Jain, B., et al. Consistency of cosmic shear analyses in harmonic and real space. 2021, *MNRAS*, 503, 3796, doi: [10.1093/mnras/stab661](https://doi.org/10.1093/mnras/stab661)
- [71] Joachimi, B., Lin, C. A., Asgari, M., et al. KiDS-1000 methodology: Modelling and inference for joint weak gravitational lensing and spectroscopic galaxy clustering analysis. 2021, *A&A*, 646, A129, doi: [10.1051/0004-6361/202038831](https://doi.org/10.1051/0004-6361/202038831)
- [72] Takada, M., & Hu, W. Power spectrum super-sample covariance. 2013, *Phys. Rev. D*, 87, 123504, doi: [10.1103/PhysRevD.87.123504](https://doi.org/10.1103/PhysRevD.87.123504)
- [73] Takada, M., & Jain, B. Cosmological parameters from lensing power spectrum and bispectrum tomography. 2004, *MNRAS*, 348, 897, doi: [10.1111/j.1365-2966.2004.07410.x](https://doi.org/10.1111/j.1365-2966.2004.07410.x)
- [74] Chisari, N. E., Alonso, D., Krause, E., et al. Core Cosmology Library: Precision Cosmological Predictions for LSST. 2019, *ApJS*, 242, 2, doi: [10.3847/1538-4365/ab1658](https://doi.org/10.3847/1538-4365/ab1658)
- [75] Navarro, J. F., Frenk, C. S., & White, S. D. M. The Structure of Cold Dark Matter Halos. 1996, *ApJ*, 462, 563, doi: [10.1086/177173](https://doi.org/10.1086/177173)
- [76] Tinker, J. L., Robertson, B. E., Kravtsov, A. V., Klypin, A., Warren, M. S., Yepes, G., & Gottlöber, S. The Large-scale Bias of Dark Matter Halos: Numerical Calibration and Model Tests. 2010, *ApJ*, 724, 878, doi: [10.1088/0004-637X/724/2/878](https://doi.org/10.1088/0004-637X/724/2/878)
- [77] Duffy, A. R., Schaye, J., Kay, S. T., & Dalla Vecchia, C. Dark matter halo concentrations in the Wilkinson Microwave Anisotropy Probe year 5 cosmology. 2008, *MNRAS*, 390, L64, doi: [10.1111/j.1745-3933.2008.00537.x](https://doi.org/10.1111/j.1745-3933.2008.00537.x)
- [78] Zuntz, J., Paterno, M., Jennings, E., Rudd, D., Manzotti, A., Dodelson, S., Bridle, S., Sehrish, S., & Kowalkowski, J. CosmoSIS: Modular cosmological parameter estimation. 2015, *Astronomy and Computing*, 12, 45, doi: [10.1016/j.ascom.2015.05.005](https://doi.org/10.1016/j.ascom.2015.05.005)
- [79] Lange, J. U. NAUTILUS: boosting Bayesian importance

- 1171 nested sampling with deep learning. 2023, MNRAS, 525, 1189
 1172 3181, doi: [10.1093/mnras/stad2441](https://doi.org/10.1093/mnras/stad2441) 1190
- 1173 [80] Gao, F., & Han, L. Implementing the Nelder- 1191
 1174 Mead simplex algorithm with adaptive parameters. 1192
 1175 2012, Comput Optim Appl, 51, 259–277, doi: [10.1007/s10589-010-9329-3](https://doi.org/10.1007/s10589-010-9329-3) 1193
 1176
- 1177 [81] Raveri, M., & Hu, W. Concordance and discordance in 1195
 1178 cosmology. 2019, Phys. Rev. D, 99, 043506, doi: [10.1103/PhysRevD.99.043506](https://doi.org/10.1103/PhysRevD.99.043506) 1196
 1179
- 1180 [82] Shi, J., Kurita, T., Takada, M., Osato, K., Kobayashi, 1198
 1181 Y., & Nishimichi, T. Power spectrum of intrinsic align- 1199
 1182 ments of galaxies in IllustrisTNG. 2021, J. Cosmology 1200
 1183 Astropart. Phys., 2021, 030, doi: [10.1088/1475-7516/2021/03/030](https://doi.org/10.1088/1475-7516/2021/03/030) 1201
 1184
- 1185 [83] van Engelen, A., Bhattacharya, S., Sehgal, N., Holder, 1203
 1186 G. P., Zahn, O., & Nagai, D. CMB Lensing Power 1204
 1187 Spectrum Biases from Galaxies and Clusters Using High- 1205
 1188 angular Resolution Temperature Maps. 2014, ApJ, 786, 1206
 1207
- 1194 13, doi: [10.1088/0004-637X/786/1/13](https://doi.org/10.1088/0004-637X/786/1/13)
 1195 [84] Siegel, J., McCullough, J., Amon, A., et al. Intrinsic 1196
 1197 alignment demographics for next-generation lensing: Revealing galaxy property trends with DESI Y1 direct 1198
 1199 measurements. 2025, arXiv e-prints, arXiv:2507.11530, 1200
 1201 doi: [10.48550/arXiv.2507.11530](https://doi.org/10.48550/arXiv.2507.11530)
 1202 Harris, C. R., Millman, K. J., van der Walt, S. J., et al. Array 1203
 1204 programming with NumPy. 2020, Nature, 585, 357, doi: [10.1038/s41586-020-2649-2](https://doi.org/10.1038/s41586-020-2649-2)
 1205 Virtanen, P., Gommers, R., Oliphant, T. E., et al. SciPy 1.0: fundamental algorithms for scientific computing in 1206
 1207 Python. 2020, Nature Methods, 17, 261, doi: [10.1038/s41592-019-0686-2](https://doi.org/10.1038/s41592-019-0686-2)
 1208 [87] Hunter, J. D. Matplotlib: A 2D Graphics Environment. 2007, Computing in Science and Engineering, 9, 90, doi: [10.1109/MCSE.2007.55](https://doi.org/10.1109/MCSE.2007.55)
 1209 Lewis, A. GetDist: a Python package for analysing Monte 1210
 1211 Carlo samples. 2025, J. Cosmology Astropart. Phys., 2025, 025, doi: [10.1088/1475-7516/2025/08/025](https://doi.org/10.1088/1475-7516/2025/08/025)